E&TR

Energy and Technology Review
Lawrence Livermore National Laboratory
November 1984

About the Cover

The energy in a high-altitude electromagnetic pulse (HEMP) can penetrate the outer surface of an electronic system through apertures and can propagate to its interior along cables, where it appears as electric currents and voltages across sensitive components. If the current or voltage exceeds the tolerance level of the electronics system, a transient disturbance or complete burn out will result. To assess the vulnerability of an electronic system to HEMP, we are concentrating on understanding the coupling of HEMP energy to the electronic system, most particularly to the interior through cables and wires. The computer-generated plot on the cover shows a result of one of the many analysis techniques we are using, an isointensity map of the total electric field induced by a plane wave incident on a slotted metallic cylinder with an axial conductor (heavy lines). The article beginning on p. 12 further discusses the phenomenology of HEMP coupling with electronic systems.

MARS: The Mirror Advanced Reactor Study

Our study has produced a conceptual design for a commercial tandem-mirror fusion reactor capable of generating 1200 MW of electricity.

At sufficiently high temperatures and densities, about 10^8 K and 3×10^{14}/cm^3, nuclei of deuterium and tritium atoms fuse to produce helium, releasing substantial energy in the process. A means of harnessing this energy would provide a virtually limitless source of electricity or other forms of power. The goal of thermonuclear research is to produce a reactor capable of generating power on a commercial scale.

The central problem in the magnetic-fusion approach is to isolate the fusion fuel, a deuterium-tritium (D-T) plasma, from the walls of a reaction chamber. Efforts at LLNL to contain hot plasmas magnetically have centered on the tandem-mirror concept, in which the plasma in a cylindrical central cell is radially confined by magnetic fields and axially confined by electrostatic potential barriers generated by thermal barrier plugs. This technique substantially reduces the axial loss of central-cell ions.

Since its inception in 1976, the tandem-mirror concept[1,2] has evolved rapidly, both experimentally[3,4] and theoretically.[5,6] The Laboratory's current experimental facilities for testing this concept are the Tandem Mirror Experiment Upgrade (TMX-U)[7] and the Mirror Fusion Test Facility (MFTF-B).[8] By 1981, it became possible to envision tandem-mirror reactors with both high power density (that is, a neutron wall load greater than 2 MW/m^2) and high power gain (that is, Q, the ratio of output plasma power to input plasma power, greater than 25).[9,10] As a result, we initiated the Mirror Advanced Reactor Study (MARS), with the objective of generating a conceptual design of a commercial fusion-power reactor based on the tandem-mirror principle.[11] The major purpose of such a conceptual reactor design study is twofold. First, it provides an economic and feasibility assessment of the reactor relevance of the physics concepts embodied in the current experimental facilities, thereby providing important feedback on the future direction of these experiments. Second, it provides a unique basis from which critical development and technology needs for future commercial fusion reactors can be assessed, thereby defining key near-term and long-term research and development tasks.

It should be stressed here that MARS represents a snapshot in time of our thinking on tandem-mirror reactors during the period from 1981 to 1983 rather than the ultimate design of a commercial fusion reactor. Indeed, at the conclusion of the study, our understanding had advanced sufficiently to enable us to envisage new opportunities for future improvement and optimization. Current reactor studies at LLNL are directed toward these ends.

MASTER

A reactor based on the tandem-mirror principle has several attractive features, including:

- Steady-state operation (no pulsed loads or cycling fatigue).
- A simple, "low-technology," linear central-cell region (the higher-technology components are located in the end cells, away from the high-power central-cell region).
- Low fluxes of charged particles to the inner wall of the central cell (less than 10 W/cm²).
- No required driving current and no identifiable plasma disruptions resulting from exponentially growing instabilities.
- Direct conversion of the energy of charged particles escaping the ends of the machine into useful electrical power.
- Natural diversion of impurities to the edge of the plasma, or halo, in the end cells.

- A high ratio of plasma pressure to magnetic-field pressure, a quantity known as beta, as a result of the machine's linear geometry. A high beta implies a high power density and therefore a lower capital cost per reactor for a given power output.

Design Objectives

The general objectives of the MARS study,[12] begun in 1981, were:

- To design efficient tandem-mirror reactors, for production of both electricity and synfuels, consistent with known physics and technology constraints.
- To identify key new physics concepts and feasible technologies that can be developed to improve reactor economics.
- To exploit the potential of fusion for improved safety, lower activation, and

The MARS tandem-mirror reactor plant for generating commercial electric power, cut away to show a portion of the reactor.
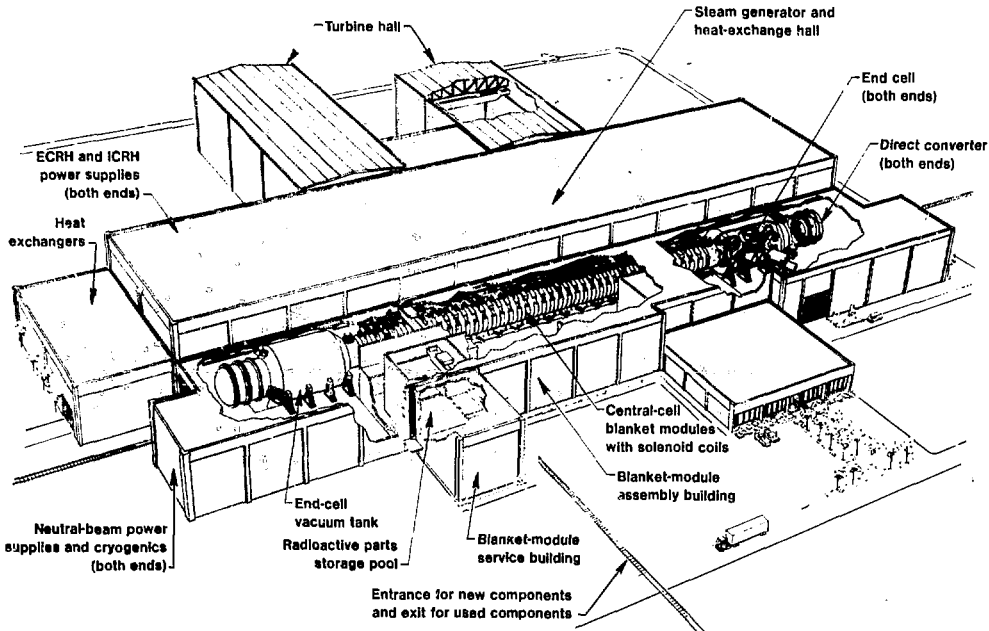
simpler disposal of radioactive wastes, compared with fission.

Additional guidelines resulted from some of our assumptions and ground rules. First, we assumed that the technology and costs are those of the tenth first-generation reactor, to be constructed about 2020. We included plug-physics concepts (thermal barriers and quadrupole plugs) that are to be tested in the TMX-U and the MFTF-B. We assumed only the additional physics and technology for improving reactor performance that should be available by 2020.

We selected structural steels that satisfy the Nuclear Regulatory Commission's (NRC's) rules for near-surface burial of Class C low-level waste. In addition, we used no flammable liquid metals in reactor blankets and required the blanket tritium inventory to be much less than 1 kg. Finally, we gave the MARS reactor the same generating capacity as today's largest nuclear-fission plants.

Key Features of the MARS Reactor Design

The heart of the MARS electricity-producing reactor (Fig. 1) is a 130-m-long cylindrical central cell designed to produce 2600 MW of fusion power in steady-state operation. Fusion of deuterium and tritium nuclei produces helium nuclei (alpha particles) and 14-MeV neutrons. Energy multiplication of these neutrons (by a factor of 1.36) in a liquid lithium-lead blanket increases the reactor's thermal power to 3350 MW, and efficient direct conversion of the plasma exhaust from the ends leads to a high net plant efficiency of 36% and a net electrical power production of 1200 MW$_e$.

Table 1 summarizes key performance specifications for an electricity-producing MARS reactor. With a total capital cost of $2.9 billion (in constant 1983 dollars), a 15% fixed interest rate, six years of construction, a 10% inflation rate, and 73% predicted plant availability, the MARS electric power plant would produce busbar electricity at about 7¢ per kilowatt-hour, which is competitive with the production cost of new electricity in

many parts of the U.S. today. Table 2 summarizes MARS reactor costs.

Because of its inherent safety and low potential for adverse effects on the environment (see below), a MARS fusion reactor should be easier to site and license than today's fission reactors. The HT-9 ferritic steel structure used in the blanket will not melt in any conceivable loss-of-coolant accident and will last

Table 1 Major performance specifications for the MARS commercial electric power plant.

Parameter	Value
Central cell	
Length, m	130
Plasma radius, m	0.49
First-wall radius, m	0.6
Neutron wall loading, MW/m^2	4.3
Fusion power, MW	2600
Plasma power gain (Q)	26
Central beta (average)	0.28
Peak central density, $10^{20}/m^3$	3.3
Blanket coolant-breeder	Lead with 17 at% lithium
Energy multiplication in blanket	1.36
Magnetic field, T	
Central cell	4.7
Choke coil (peak)	24[a]
Yin-yang mirror (peak)	7.5[b]
Net electric power produced, MW$_e$	1200
Recirculating power fraction	0.22
Total magnet stored energy, GJ	49

[a]Sum of 16 T from outer superconducting coil and 8 T from copper insert coil.
[b]Field on the conductor, 10 T.

Table 2 Summary of capital costs for the MARS commercial electricity-generating fusion power plant.

Item	Cost, $ million (1983 dollars)
Land and land rights	5
Structures and facilities	250
Reactor system	1517
Turbine plant	275
Electrical plant	160
Other	33
Special materials	125
Construction equipment and services	240
Engineering and management	189
Other	118
Total	2912

at least five years before scheduled replacement. Because almost all of the radioactive material formed in the steel is short-lived (less than five years), the spent blanket modules can simply be filled with concrete and buried on site. In addition, the blanket coolant (lead mixed with 17 at% lithium enriched to 90% lithium-6) will not burn in either air or water. As tritium produced in the blanket coolant is continually extracted at a constant rate, it eventually reaches an equilibrium concentration. Under steady-state tritium processing conditions, the equilibrium amount of tritium in the coolant is extremely low (less than 8 g in 1400 tonnes of coolant).

Many of the plasma-confinement and magnet-design features of the MARS reactor are derived from recent tandem-mirror experiments, notably the MFTF-B and the TMX-U. The yin-yang magnets are simply scaled up from the superconducting niobium-titanium magnets used in the MFTF-B, minimizing technical risk (Fig. 2). The plasma model[13] used to design the end cell of the MARS reactor has accurately predicted much of the behavior we have observed experimentally in the TMX-U. These predictions include:

● Microstable sloshing ions with loss rates that can be calculated using Fokker-Planck codes.

Fig. 2

Cutaway view of one MARS reactor end cell (center) and adjoining portion of the central cell (left).

4
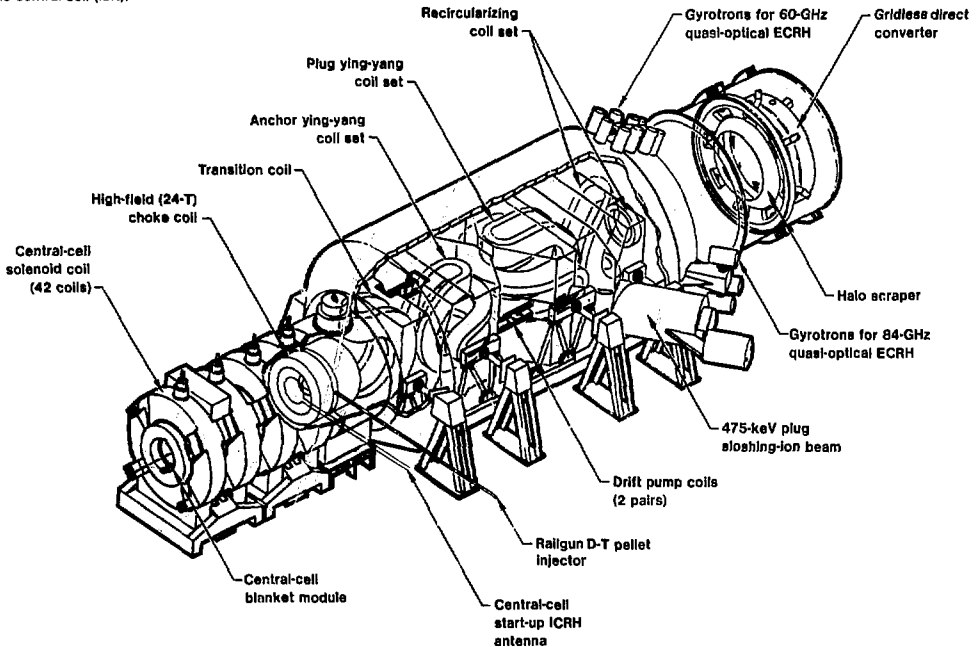
• The formation of an enhanced potential barrier by electron-cyclotron resonance heating (ECRH).

• Successful plugging at the ends of the central cell, suppressing ion losses there to the point where radial ion losses dominate.

• Net collection of electron current on end-wall plates

• Improved vacuum pumping by the plasma halo.

The TMX-U experiment will soon include tests of such unique MARS reactor features as drift pumps and high-field choke coils.

To fuel the central-cell fusion plasma, we plan to inject 6.5 pellets of solid D-T per second, each with a mass of 0.01 g, at high velocity (20 km/s). Nearly all the 3.5-MeV alpha particles formed in the fusion reactions are trapped by the high-field (24-T) choke coils at each end of the central cell, permitting the D-T fuel to absorb most of their energy. Because of high positive potential barriers (more than 150 keV) in the end cells, the resulting heating of the D-T plasma can sustain the small axial and radial energy losses from the central cell, enabling the fuel there to burn in a self-sustaining fusion reaction. Thus the central cell needs auxiliary heating only during start-up.

Under these circumstances, the power-gain factor Q increases almost linearly with the length of the central cell. For the MARS reactor, we chose a central-cell length (130 m) that will produce 1200 MW of electric power, which yields a Q of 26.

The thermal barriers[5] that moderate the power required for end-plug heating are maintained by both ECRH power and drift pumping.[14] This latter technique uses low-frequency rf fields to induce ions trapped in the thermal barrier to escape radially. Because these ions will be replaced by collisional trapping of ions from the central cell, the fusion burn there can be controlled by modulating the drift pumping.

Because of drift pumping and the high plugging potentials, nearly all of the trapped D-T ions, helium (fusion ash), and other impurities escape by radial diffusion to the plasma edge (halo) in the

end cell, where they are removed by an annular halo scraper (Fig. 3). This mechanism acts as a high-speed vacuum pump, minimizing ion heating of the first wall and ion sputtering in the central cell.

The plasma electrons are left to escape along the field lines and are collected inside the halo scraper by end plates biased to minus 167 kV. This electron collection directly generates almost enough dc electricity (about 300 MW$_e$) to power the plug heating and plant auxiliary equipment. Because the radial loss of end-plugged ions eliminates the need for suppression grids,[15] we can make the high-power, electron direct converter small enough to fit in a vacuum tank 10 m in diameter, like that used on the MFTF-B.

Several new but developable technologies in the MARS reactor design (summarized in Table 3) are keys to its performance. The lithium-lead blanket itself is very simple and rugged, and the

Fig. 3

Cutaway view of system for converting the energy of ions and electrons lost from the plasma ends into electric power. The system also intercepts impurity and drift-pumped ions in the outer halo of the plasma and pumps them away.
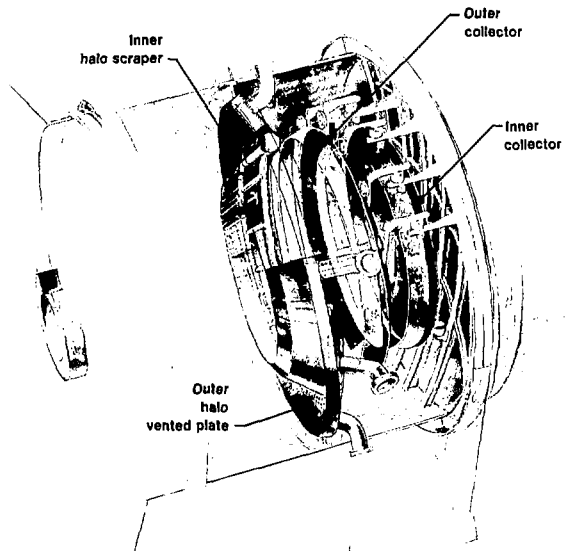
remotely replaceable modules (Fig. 4) weigh only 2.7 tonnes each when drained. Scheduled module replacement (every five years) requires only 11 days of downtime. Critical technologies for this blanket design are double-walled tubes in the heat exchanger to keep tritium permeation into the steam cycle below 10 curies per day and cold traps to reduce the concentration of corrosion products in the main heat-transfer loop. Most of the tritium vulnerable to release as gaseous T_2 is in the tritium purification and separation system (about 160 g) and in the pellet-injection system (about 20 g).

The Plant

Most of the MARS power plant shown in Fig. 1 is conventional. However, the general arrangement of buildings and functions takes into account the linearity of the tandem mirror and uses the open access to advantage. One side of the central cell contains all facilities for removing, storing, and replacing spent equipment, and the other side contains the energy conversion systems. The single unique feature, aside from the fusion reactor, is

the use of two independent power cycles, one with superheated steam and the other with saturated steam.

The safety-related buildings in the MARS facility are the reactor hall, the steam-generator hall, the hot cell, the spent-blanket pool, the tritium building, the control building, and the diesel-generator building. All of these safety-related buildings are designed to sustain earthquake forces, tornado-generated winds and missiles, accident pressures and temperatures, and operating loads.

The MARS electrical systems are designed to interface with the electric utility grid and to provide standby emergency power and auxiliary power for start-up and normal operation. The dominant users of recirculating power, which totals 334 MW, are the supplemental plasma heating systems (158 MW) and the resistive magnets, including drift pumps (101 MW).

Maintenance

The maintenance design objectives for the MARS reactor are:

● To be able to do all maintenance by remote control but with enough shielding to permit hands-on operations at the outer surface of the reactor.

● To minimize down time for scheduled maintenance.

● To be able to replace, quickly, any reactor component that fails unexpectedly.

Gate valves close off the end cells when the central cell is opened, and temporary shielding protects personnel in the area of the end cell. Two major systems that require periodic replacement are the blanket modules and the normal conducting choke-coil inserts. We have developed detailed schedules for servicing these systems.

We have designed the system to accommodate remote replacement of any component, including such major (and long-lived) items as yin-yang and central-cell coils. The central cell is segmented into sections—each of which contains two magnet coils and an associated blanket, reflector, and shield modules—that can be removed on permanent rails embedded in the floor. The end-cell

Table 3 Critical technologies for the MARS reactor requiring research and development.

Technology	Requirement
Negative-ion beam	475 kV, 10 A, 0.1 A/cm^2
High-field hybrid magnet	24-T, 60-cm bore; outer superconducting solenoid (16 T)—Nb$_3$ Sn, NbTi; inner normal conducting solenoid (8 T)—copper alloy
Drift pumping	18 kA, 47 kHz, $\Delta f/f = 0.4$
Direct converters, plasma exhaust	3-MW/m^2 gridless, compatible with radial potential control; high recycling halo dumps to pump 2-kA D-T and helium
High-speed fuel pellet injector	20 km/s, 6.5 Hz, pellet radius 2 mm
Quasi-optical ECRH systems	42-MW, 60-GHz, 2.5-MW gyrotron tubes
Lithium-lead blanket	T_{max}, 500°C; S_w, 5 W/cm^2; 0.1 mm/year erosion, wall loading greater than 4 MW/m^2; corrosion-product cold traps
Double-wall heat exchanger	10^{-4} attenuation of T_2 from coolant side to steam side

magnets can be pulled out axially with the same tractors used during initial installation. All superconducting magnets are designed as lifetime components and will require replacement only in the unlikely event of a failure.

Operation

Operation of the MARS power plant consists of preoperational testing, initial commissioning, start-up, operation and testing at fractions of full power, steady-state operation, and shutdown. Four phases of operation are repeated over the life of the reactor:

I—Start-up, either cold or hot.

II—System testing, plasma initiation, and standby operation at less than 5% of rated power.

III—Staged power ascension at several levels.

IV—Operation at full rated power.

The start-up of the MARS power plant is similar to that of other power plants, fossil-fueled or nuclear, except for the special requirements of the plasma system and the liquid-metal blanket. The liquid-metal blanket needs special start-up procedures to prevent thermal shock and stress to the system during a cold

start. The only additional system needed for the blanket is a source of heated helium.

Hot helium is circulated through the primary loop for about 30 hours to preheat it to a uniform temperature of 350°C. The molten lithium-lead mixture is then pumped in from the storage tank to fill half the primary loop, followed by the blanket from bottom to top, and finally the rest of the primary loop. Start-up from a hot shutdown is expected to be much simpler and faster.

In phase II, much of the activity will be associated with plasma and plasma systems, including supplemental heating, drift pumping, and testing of the direct converter. These tests will be performed with the power as low as possible.

During staged power operation (phase III), turbine-trip, loss-of-load, and loss-of-flow tests will be performed at each power level (including 100%) to validate safety-analysis models and to collect data on performance under these transient conditions. We would also measure flow conditions, strain-gauge data, and vibrations, and monitor in detail coolant chemistry and radioactivity, neutron leakage, and corrosion data.

Fig. 4

Shield and built-in reflector

Coolant head

Lid

Tubes (17 rows)

Beams (10 rows)

Liquid breeder coolant (17 at% lithium, 83 at% lead)

HT-9 ferritic steel structure
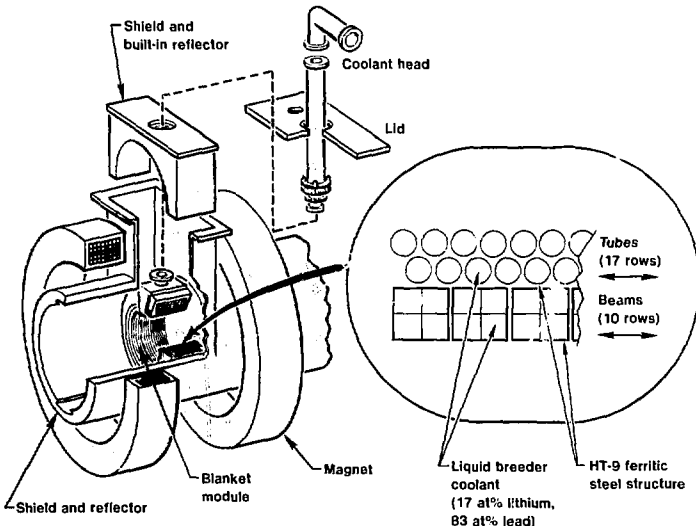
Magnet

Blanket module

Shield and reflector

Section of the MARS reactor central cell, showing construction details of the lithium-lead blanket modules.

Environment and Safety

The MARS reactor is designed to minimize adverse effects on the environment and for general passive safety (only minimal active measures are required for safe operation). Normal and accidental release of radioactive material, exposure of workers, and waste management problems have all been minimized by selection of appropriate materials and operational parameters.

Radioactivity (and the accompanying possibility of exposure) affects a number of issues. Among these are:

• Afterheat (residual heat generated after the fusion reaction is shut down) from induced radioactivity in the blanket, reflector, and shield.

• Coolant activation.

• Biological dose to workers outside the central-cell shield and the end-cell shields.

• Management of radioactive waste.

Afterheat is the principal source of energy that must be removed in case of accidental loss of coolant or loss of flow in the blanket. It starts out at 4% of the steady-state thermal power and drops off rapidly because most of it comes from manganese-56 (2.58-hour half-life). Our analysis shows that the blanket will not melt even in the worst combination of loss of flow and loss of coolant.

Electrolytic lead in the coolant contains 0.0042 wt% bismuth, which on exposure to neutrons becomes polonium-210, a volatile emitter of 5.3-MeV alpha particles with a 139-day half-life. Lead itself also becomes a source of polonium-210 after double neutron capture. The initial production rate of polonium-210 in the MARS reactor coolant will be 6 mCi/s, and the equilibrium level after a few months of steady operation could be as much as 20 kCi, depending on the chemistry of polonium in the lead-lithium mixture. Fortunately, polonium-210 is volatile enough to permit its continuous removal in the tritium-recovery system.

To minimize biological dose, we have designed the central-cell shield so that a person working at the surface 36 hours after shutdown will receive less than 100 mrem per work week. One feature that helps make this possible is an outer shield of aluminum. The parts of the end-cell tank that are internally shielded by magnets and other massive structures are safe to approach immediately after shutdown. Concrete shielding 65 cm thick on the rest of the tank permits access within 48 hours.

One of our design goals was to make all components comply with NRC regulations for disposal of radioactive fission wastes by near-surface burial. For example, we chose ferritic steel because it is low in the nickel, niobium, and molybdenum that contribute strongly to induced radioactivity in austenitic steels. As a result, we can dispose of a spent blanket as class-C waste in a near-surface burial site by encasing it in concrete after a short cooling-off period.

Special steel alloyed with molybdenum depleted in its isotope 92 (the only one that produces long-lived waste) would be more expensive, adding 13% to the cost of the blanket. However, it would virtually eliminate long-lived radioactivity. We could then compact the blanket to 7% of its volume and dispose of it as class-C waste, even without concrete encasement. No previous steel blanket design achieves this low level of activation.

The coolant, as extracted from the reactor, would qualify for class-C disposal upon chemical processing to remove 96% of the radioactive silver and bismuth.

Nickel-63, produced by neutron capture in the copper of the choke-coil insert, has a half-life of about 90 years. This makes the insert unsuitable for immediate near-surface burial. It is small enough for economical deep geologic burial; however, it would qualify for class-C disposal after storage for 360 years.

The MARS power plant has been designed to meet present NRC regulations for fission plants regarding normal radiation dose at the site boundary. (The NRC has not yet set explicit limits on tritium release from fusion power plants.) Direct radiation from the plant is expected to be innocuous. Tritium released up the stack is less than 15 curies per day; the resulting dose at the site boundary

is negligible. Loss through the heat exchangers, which does not go directly to the environment, is less than 10 curies per day, assuming oxidation of tritium in the gap between the double-walled tubes.

We also performed a safety analysis for accidental dispersal of activated (radioactive) structure, activated corrosion products, activated coolant, and tritium. In many cases, we could identify no credible way that release could occur but calculated doses anyway in the event that a mechanism is discovered. Even should the filtering systems fail, the doses at the site boundary are still well below 25 rem, the present NRC guideline for fission plants (Table 4).

Power Flow and Cost Scaling

The MARS plant makes very efficient use of the fusion energy it produces because of its:

● High multiplication of neutron energy in the blanket.

● Direct conversion of plasma end losses to electricity.

● High-efficiency thermal conversion.

● High plasma gain.

● High-efficiency supplementary heating of plasma.

Starting with the supplemental heating power absorbed by the plasma (100 MW) and applying the Q factor (26) yields a fusion power of 2600 MW. Energy multiplication in the blanket raises the total to 3460 MW.

Of this total, 70 MW is lost to synchrotron radiation from the end plugs and from neutrons that do not enter the blanket. The rest is divided among the blanket (2090 MW), the reflector (730 MW), and the end cells (570 MW). The blanket heat is converted (with an efficiency of 42.7%) in the superheat cycle, producing 890 MW of electricity. Some of the end-cell power is directly converted to produce 290 MW of electricity; the rest is combined with heat from the reflector in the saturated-steam cycle (efficiency 34.3%) to produce 350 MW of electricity.

The sum of these three electrical outputs is 1530 MW$_e$, but 330 MW must be recirculated to the plant. Of this

recirculating power, 160 MW goes to the plasma-heating systems, 100 MW to run the normal-conducting magnets, and 70 MW to run the auxiliary plant equipment. Subtracting the recirculating power, we obtain a net output of 1200 MW$_e$.

This power balance could be improved at several points. Oscillator tubes under development could be used to make more efficient ion-cyclotron resonance heating (ICRH) transmitters, saving 6 MW. Increasing the field in the superconducting portion of the hybrid choke coil to 18 T would reduce the magnet power by more than 20 MW. Newer, more efficient cryogenic equipment could save 3 MW. Increasing the fraction of energy captured in the blanket could generate an additional 30 MW. Thus, without changing the physics, plasma configuration, and most subsystems, we could generate an additional 60 MW.

The shape of the tandem-mirror reactor gives it a strong economy of scale. As we lengthen the central cell, the fusion power increases linearly, but the cost of the end cells and the recirculating power remains nearly constant. A 1700-MW$_e$ plant thus costs only 14% more than the 1200-MW$_e$ plant we have described. Per unit of electricity generated, a 2000-MW$_e$ plant would cost 25% less than the 1200-MW$_e$ MARS design.

There is considerable interest today in smaller fusion power plants. However,

Table 4 Radiation dose at the site boundary of the MARS plant under worst-case conditions.

	Dose, mrem	
Material released	Containment intact	Containment breached
Activated structure		
Full blanket	0.032	100
One module	0.0012	4.6
Activated corrosion products	0.8	2 600
Tritium in pellet injector	0.06	16
Activated coolant	—	24
Current NRC guidelines, fission power plants		25 000

9

a small reactor obtained by simply shortening the central cell, keeping everything else in the MARS design the same, would be prohibitively expensive. We are currently pursuing alternative design concepts, using compact octopole end plugs, for affordable tandem-mirror fusion reactors that produce less than 600 MW.

Future Directions

Table 3 identifies some of the technologies that are critical if the MARS reactor is to achieve its performance goals. Extensive research and development will be needed on each of these items.

Although the MARS reactor represents a significant advance in tandem-mirror reactor design, it is still at an early stage of conceptual development and will continue to evolve as new experiments and better ideas are brought to bear. It took almost two years to identify the many physics and engineering requirements of the MARS design. Now, at the conclusion of the study, we can already see at least four general areas in which to seek future improvement and optimization of tandem-mirror reactors.

We can probably find a better trade-off between central-cell field, wall loading, and end-cell heating power. Some of our recent post-MARS analyses indicate that halving the wall loading (and reducing the central magnetic field from 4.7 to 3.3 T) could virtually eliminate synchrotron radiation, reducing total plug power by a factor of four and almost doubling Q.

Preliminary investigations suggest that proper design can improve the neutron tolerance of superconducting magnets by a hundredfold. This would reduce the thickness of the shielding required by 20 to 40%, making it possible to move the magnet windings closer to the axis. Magnet volume, stored energy, weight, and cost could thereby be reduced by a factor of two to three.

One way to simplify the main heat-transfer system and the balance of the plant would be to find a way to use only one coolant in the blanket instead of two. This would enable relocation of the

heat exchangers closer to the reactor vault and would save money on piping and turbines. Reducing the lithium isotopic enrichment would also reduce the inventory cost of the coolant. In addition, there may be better coolants than water for capturing heat in the end-tank converters.

Theoretical efforts are underway, here and elsewhere, to find ways of reducing the size and cost of the end plugs. Preliminary indications are that essentially single-mirror cells that are less than one-fourth the length of the MARS reactor end cells may prove effective. They do, however, require alternative methods of plasma magnetohydrodynamic stabilization. Such a development, coupled with magnet designs of higher efficiency, might halve the cost of reactor-plant equipment.

Although such avenues for future improvement are now being vigorously explored, many of the physics and engineering concepts used in the MARS design will endure in future tandem-mirror reactor designs. These include the central cell with its engineering simplicity and high-performance blankets, the high-field choke coils, the drift-pumping concept, the sloshing-ion thermal barriers, the quasi-optical ECRH systems, and the negatively biased direct converters.

The real value of the MARS, like that of all previous reactor studies, is educational. It lies in the problem-solving entailed, in the new concepts engendered by the effort of designing at the leading edge of technology, and in providing direction to near-term plasma-physics research. In this respect, MARS is an invaluable step toward the the design of commercial fusion power plants. ⊡

Notes and References

1. G. I. Dimov, V. V. Zakaidakov, and M. E. Kishinevsky, in *Proc. Sixth Intl. Conf. on Plasma Physics and Controlled Nuclear Fusion Research, Berchtesgaden, West Germany, 1976*, International Atomic Energy Agency, Vienna, Austria. Paper No. C4 (1977).

2. T. K. Fowler and B. G. Logan, *Comments Plasma Phys. Controlled Fusion* **2**, 167 (1977).

3. T. C. Simonen, Ed., *Summary of TMX Results—Executive Summary*, Lawrence Livermore National Laboratory, Rept. UCRL-53120 (1981); see also T. C. Simonen *et al.*, "Plasma Confinement Experiments in the TMX Tandem Mirror," in *Proc. Intl. Conf. Plasma Phys. and Contr. Nucl. Fusion Res., 8th, Brussels, 1980*, International Atomic Energy, Vienna, Austria, Rept. IAEA-CN-38/F-1 (1981).

4. T. C. Simonen *et al.*, *Initial TMX-U Thermal Barier Experiments*, Lawrence Livermore National Laboratory, Rept. UCID-19872 (1983); see also D. P. Grubb *et al.*, *Thermal Barrier Production and Identification in a Tandem Mirror*, Lawrence Livermore National Laboratory, Rept. UCRL-90536 (1984).

5. D. E. Baldwin *et al.*, "Studies in Tandem Mirror Theory," in *Proc. Intl. Conf. Plasma Phys. and Contr. Nucl. Fusion Res., 8th, Brussels, 1980*, International Atomic Energy Agency, Vienna, Austria, Rept. IAEA-CN-38/FI (1981), Vol. 1, p. 133.

6. R. H. Bulmer *et al.*, "Gyrokinetic Equilibrium and Stability in Quadrupole Tandem Mirrors," in *Proc. Intl. Conf. Plasma Phys. and Contr. Nucl. Fusion Res., 9th, Baltimore, Maryland, 1982*, International Atomic Energy Agency, Vienna, Austria, Rept. IAEA-CN-41/G-2, Vol. 1, p. 531 (1982).

7. T. C. Simonen *et al.*, "TMX Tandem Mirror Experiments and Thermal Barrier Theoretical Studies," in *Proc. Intl. Conf. Plasma Phys. and Contr. Nucl. Fusion Res., 9th, Baltimore, Maryland, 1982*, International Atomic Energy Agency, Vienna, Austria, Rept. IAEA-CN-41/G-2, Vol. 1, p. 519 (1982).

8. R. R. Borchers and C. M. Van Atta, *The National Mirror Fusion Program Plan*, Lawrence Livermore National Laboratory, Rept. UCAR-10042-80 (1980).

9. G. L. Kulcinski *et al.*, "A Commercial Tandem Mirror Reactor Design with Thermal Barriers—WITAMAR I," in *Proc. ANS Topical Meeting on the Technology of Contr. Nucl. Fusion, 4th, King of Prussia, PA, Oct 14-17, 1980*, University of Wisconsin, Madison, Wisconsin, Rept. UWFDM-375 (1980).

10. G. A. Carlson *et al.*, *Comparative End-Plug Study for Tandem Mirror Reactors*, Lawrence Livermore National Laboratory, Rept. UCID-19271 (1981).

11. An alternative reactor design studied, not discussed here, is capable of generating enough hydrogen to produce 38 000 barrels of synthetic fuel a day.

12. We conducted the MARS for the U.S. Department of Energy with TRW as the prime industrial partner, General Dynamics, EBASCO Services, and Science Applications as subcontractors, and the University of Wisconsin as a university partner. Grumman Aerospace contributed significantly to the engineering effort, with additional support from the University of California at Los Angeles and Ontario Hydro; see *Mirror Advanced Reactor Study (MARS)—Final Report*, Lawrence Livermore National Laboratory, Rept. UCRL-53480 (1984). See also, "Mirror Advanced Reactor Study (MARS)—Executive Summary and Overview," Lawrence Livermore National Laboratory, Rept. UCRL-53333 (1984).

13. R. B. Campbell, *TMRBAR—A Code to Calculate Plasma Parameters for Tandem Mirror Reactors Operating in the MARS Mode*, Lawrence Livermore National Laboratory, Rept. UCID-19875 (1983).

14. D. E. Baldwin, *Bull. Amer. Phys. Soc.* **2**, 1021 (1981); see also B. G. Logan, *Mirror Advanced Reactor Study Interim Report*, Lawrence Livermore National Laboratory, Rept. UCRL-53333 (1983).

15. W. L. Barr and B. G. Logan, "A New Direct Converter for Tandem Mirror Reactors," *Comments Plasma Phys. Controlled Fusion* **8**(3), 103 (1984).

Electromagnetic Coupling of High-Altitude, Nuclear Electromagnetic Pulses

We have used scale models to measure the predicted coupling of electromagnetic fields simulating the effects of high-altitude nuclear electromagnetic pulses on the interior surfaces of electronic components.

For further information contact
Briar Cabayan (415) 422-8871.

The potential hazard of nuclear-generated electromagnetic pulses (EMP) was first recognized by the U.S. twenty years ago. During the 1962 Fishbowl test series above Johnston Island, electromagnetic effects of a high-altitude nuclear detonation (Starfish Event) were observed 1300 km away in Hawaii. These observations provided a vivid illustration of the far-reaching consequences of EMP and helped to stimulate interest in understanding the origin and quantifying the vulnerability of electronic systems to EMP.

It is now widely known that high-altitude EMP (HEMP) is produced by the downward-directed gamma rays from a high-altitude nuclear explosion. At altitudes of 20 to 50 km, the gamma rays scatter in the earth's atmosphere, producing a current of Compton electrons. The electrons are deflected by the earth's magnetic field, establishing

a Compton current transverse to the direction of the incident gamma-rays. This transverse current is the source term in Maxwell's equations that drives the radiated electromagnetic fields. Since the gamma rays travel at the speed of light, the transverse currents generated at different positions along the line connecting the nuclear burst and an observer on the ground radiate like a phased array of antennas. The electromagnetic signals from separate current elements arrive at the ground simultaneously to produce an intense, short burst of electromagnetic energy.

The EMP produced by an exoatmospheric nuclear explosion depends on the height of burst and the orientation of the geomagnetic field lines. In addition, features of the nuclear source that determine the magnitude of the EMP include the gamma-ray yield, rise time, and energy spectrum. As an

example of the far-reaching effects of HEMP, a single burst at an altitude of 400 km over the continental United States would have a ground range of 2200 km. The maximum electric-field intensity occurs just south of surface zero and can be as high as 50 kV/m. The spectrum extends from essentially dc frequencies to several hundred megahertz.

High-altitude explosions are not the only means of generating EMP. Asymmetric Compton currents produced by near-surface or low-altitude bursts can also generate EMP. However, the EMP produced by a high-altitude burst covers much more extensive areas with high field strengths and therefore provides a more taxing threat model for hardening electronics.

A HEMP interacts destructively with many military electronics systems. The energy in a HEMP can penetrate a system's outer surface through apertures and propagate to its interior along cables, finally appearing as electric currents and voltages across sensitive components of electronics subsystems. If the current or voltage exceeds the tolerance level of an electronics system, the system will either suffer a transient disturbance or burn out completely. An understanding of this coupling phenomenon and the development of predictive tools would provide the framework for a more scientific approach to evaluating the effects of HEMP and designing hardened systems.

To assess the vulnerability of a complete system to HEMP, we must examine three areas of HEMP-system interactions: component and subsystem susceptibility, system vulnerability, and coupling with HEMP (Fig. 1). In identifying component and subsystem

susceptibility, we are focusing on one-, two-, and (possibly) three-dimensional computer models that include the major physical phenomena, as represented, for example, by heat and electronic transport equations.[1] To identify system vulnerabilities and to point the way to effective hardening, we are applying probabilistic failure analysis. Finally, in assessing coupling, our goal is to achieve a phenomenological understanding based on a multifaceted, complementary approach that combines analytical, computational, and experimental techniques, including scale-model tests. We describe here our current work on coupling phenomenology.

Coupling Phenomenology

The general coupling problem is to predict the currents and voltages induced at critical subsystems by an incident electromagnetic field. Much of the past emphasis has focused on the development of tools for assessing exterior coupling. As a result, fairly accurate techniques are available for predicting induced charges and currents on the exterior envelope of systems. Such is not the case for tools to evaluate coupling through apertures to internal cables, wires, and leads. Our investigations therefore focus on the phenomenology of interior coupling.

We are developing investigative tools, consisting of formal analysis, computer models, and laboratory experiments, to predict internal stresses (currents and voltages) induced by incident HEMP in sensitive electronic components of

Fig. 1

Three related steps are involved in assessing the vulnerability of a complete system to HEMP: determining component and subsystem susceptibility, assessing the coupling effects of HEMP, and defining a statement of system vulnerability or hardening. The coupling problem involves determining the transfer function between the environmental and stress parameters for a given system.
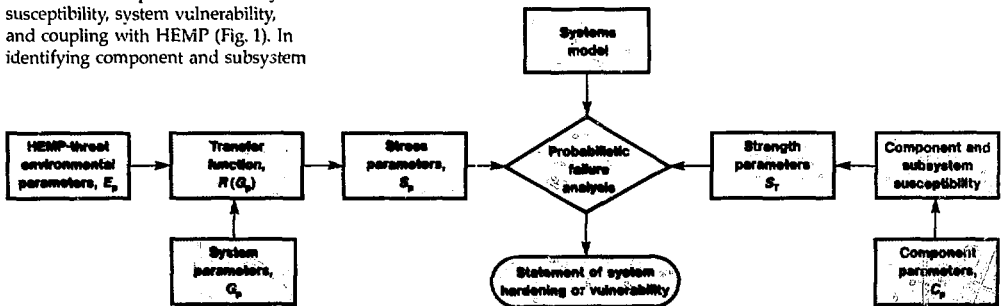
military systems. In addition, the tools will:

• Provide designers with criteria for designing hardened systems.

• Help us evaluate various hardening options for existing systems.

• Help us extrapolate the available data base to threat-parameter regimes unattainable with present simulators.

To bridge the gap between the physics of electromagnetic phenomena and empirical, full-system test data, our approach applies increasingly sophisticated assessment tools to objects of growing complexity. Figure 2 illustrates the progression from a simple (canonical) object, to a generic object, and finally (in this example) to a specific aircraft.

Typically, the object with which an incident electromagnetic field interacts has an exterior envelope that is either metallic or made of composite materials. The envelope is usually punctuated with apertures and penetrating conductors. The interior of the object consists of separate compartments with connecting cable bundles. Unlike the exterior

Canonical

Generic

Specific

Fig. 2

Progression from canonical objects to generic objects to a model of a specific aircraft.

14

features (which can be defined with an acceptable degree of precision), the interior features are extremely complex and very hard to quantify electromagnetically.

The coupling problem is characterized by two sets of parameters (see Fig. 1):

• Environmental parameters E_p specifying the amplitude, frequency, polarization, and angle of incidence of the electromagnetic pulse.

• Interior stress parameters S_p, describing electric and magnetic fields interior to the system envelope, cable short-circuit currents and open-circuit voltages, and currents and charges on internal surfaces.

The solution to the coupling problem, given a set of system parameters G_p, requires specification of the transfer function $R(G_p)$ between the environmental and stress parameters.

The two sets of parameters are related to each other by Maxwell's equations with appropriate boundary conditions for a given system parameter descriptor, G_p. By virtue of increasing complexity, G_p can denote the full range from the simplest generic object (a spherical or cylindrical cavity with apertures and cables) to the actual object in its full-blown complexity.

The objective of each of the three techniques (formal analysis, computation, and laboratory testing) is to develop the transfer function, $R(G_p)$, a mathematical model that relates the interior stress parameters, S_p, to the environmental threat parameters, E_p. In each case, $R(G_p)$ depends on the system parameter descriptor, G_p, and will increase in complexity as the system itself becomes more complex.

We investigate the coupling problem in a "bottom-up" manner, starting from the least complex and progressing through increasingly more complex system parameters. At each stage, we must estimate the appropriate transfer function and how it changes with each increase of complexity.

Figure 3 shows the regions of applicability of the three techniques to objects of various degrees of complexity. To bridge the gap between the scale model and the full-scale system, we
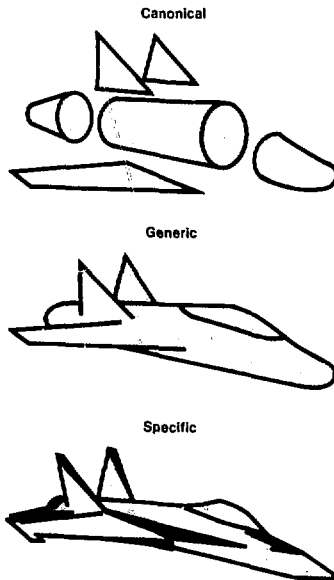
introduce a system mock-up. This is a structure that embodies a fair degree of the actual system's complexity but has been constructed according to very strict design plans—that is, the system definition can be performed with certainty. Although we will not further discuss simulation tests of system mock-ups and systems, we mention them to indicate how phenomenological investigations complement and tie into empirical tests.

Formal Analysis

Our techniques of formal analysis treat simple interior-coupling problems, such as spherical cavities with apertures and cylinders with slits, with extreme rigor.[2] Past analyses of aperture coupling have relied heavily on approximate theories such as the quasi-static Bethe hole theory. These are inadequate models except for very low frequencies.[3]

These techniques lead to exact solutions to a large class of canonical aperture-coupling problems—those in which the scattering object coincides with a constant-coordinate surface in a separable geometry. Problems that can be treated include an electric- or magnetic-polarized plane wave incident at an arbitrary angle on an infinite (perfectly conducting) cylinder with an arbitrary number of infinite axial slots enclosing a concentric impedance surface or a set of infinite axial wires. Another treatable problem is a sphere with a circular aperture enclosing a concentric impedance sphere or a set of dipoles.

In our new aperture coupling description, the components of the electric and magnetic fields tangential to the scattering body are expanded in the eigenmodes corresponding to that object. Satisfaction of the electromagnetic boundary conditions then leads to a system of n-series equations. This system is solvable using techniques developed for the classical Riemann-Hilbert problem of complex-variable theory. Once the modal coefficients are known, the field components and the currents on the metal can be computed. In contrast with other approaches, the singular behavior near the edges of the aperture

can be handled analytically for object dimensions that are small or large relative to the wavelength of the incident field.

Figure 4 shows one such result using our formal techniques to evaluate coupling to a slit cylinder with a center conductor. The diameters of the cylinder and the wire are 2.0 and 0.2 wavelengths, respectively. The field is incident into the aperture from the left, with the electric-field vector parallel to the axis of the cylinder. The contours indicate regions where the ratio of the total field to the incident field is of equal intensity. The colored areas show regions of enhanced field intensity, with a maximum (indicated by the cross just to the left of the axial conductor) as high as a factor of 2.6.

This example clearly demonstrates the utility of formal analysis. The results can be obtained for any environmental parameter, E_p, incident field amplitude, frequency, polarization, and angle of incidence. Consequently, we can study variation in internal stress parameters, S_p, such as electric and magnetic fields interior to the object and currents, and charges on any interior surfaces, as a function of the environmental

Fig. 3

The coupling phenomenology approach involves increasingly more complex assessment tools treating increasingly more complex objects. The simplest objects are canonical, and the most complex are full-scale systems.
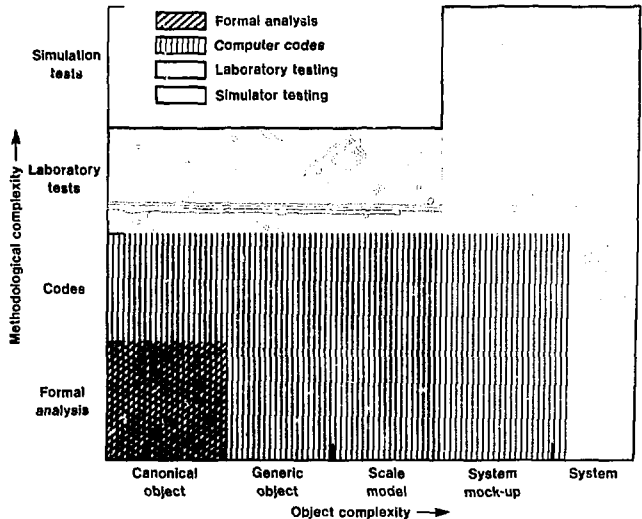
parameters. Those results can then be used to validate various numerical analyses. Moreover, we can derive from formal analyses general engineering rules of thumb that are applicable to generic objects of the same class.

Computational Approaches

Two numerical approaches to the HEMP problem are possible: surface integral equations and finite-difference or finite-element approaches. Integral equations have been applied very extensively to solve the exterior coupling problem and, in a few instances, to the interior coupling problem. However, for interior coupling, finite-difference and finite-element codes show the most promise for prediction. Of these, finite-difference codes have been applied to system-like interior geometries, but their accuracy has not yet been determined. However, we have shown that this approach yields reasonably accurate interior response predictions when compared with

experiment (typically within ± 3 dB of the resonant peaks, which characterize the interior response, and within ± 6% in frequency for the same peaks).

We expect that in the future, either finite-difference or finite-element codes will be capable of modeling complex system-like interiors down to the bulk-cable level. Beyond that, it will be necessary to adopt hybrid approaches to modeling individual cables in a bundle, implemented in transmission-line codes and in finite-difference and finite-element codes. The transmission-line code can model the bundles and is connected mathematically to the finite-difference or finite-element grid.

Figure 5 graphically displays the various codes in terms of objects that have been modeled and experimentally validated. Note that in contrast to exterior coupling studies, interior coupling studies are still in their infancy.

Surface Integral Equations

The electric-field integral equation, deduced from the Maxwell field equations and the boundary conditions, is particularly convenient for modeling wire structures since it can be reduced to a one-dimensional equation for thin wires. Aperture coupling can be modeled with this technique if the surface is modeled as a wire grid of sufficiently fine mesh size. We have used the technique to write a numerical electromagnetics code specifically for modeling antennas on structures such as ships or aircraft.[4] The code can also be applied to some aperture-coupling problems.

The integral equation is solved numerically by the method of moments, wherein the current is represented as a sum of N basis functions and the equality is enforced on N weighted integrals of the equation. The resulting N linear equations are then solved for the coefficients in the current expansion.

This code includes a number of options such as finite conductivity, transmission lines, and a provision to add wires to a model without repeating the entire solution. For an accurate solution, the lengths of segments must be less than about 0.1λ (the wavelength

Fig. 4

Formal-analysis techniques produced this isointensity map. A plane wave is incident from the left on a slit cylinder with an axial conductor. The electric-field vector is parallel to the axis of the cylinder. Contours indicate regions where the ratio of the total to the incident field is of equal intensity. The colored regions are areas of enhanced field intensity, with a maximum (indicated by the cross just to the left of the axial conductor) as high as a factor of 2.6. The predicted enhancement agrees with the results of analogous experiments reported by others.

16
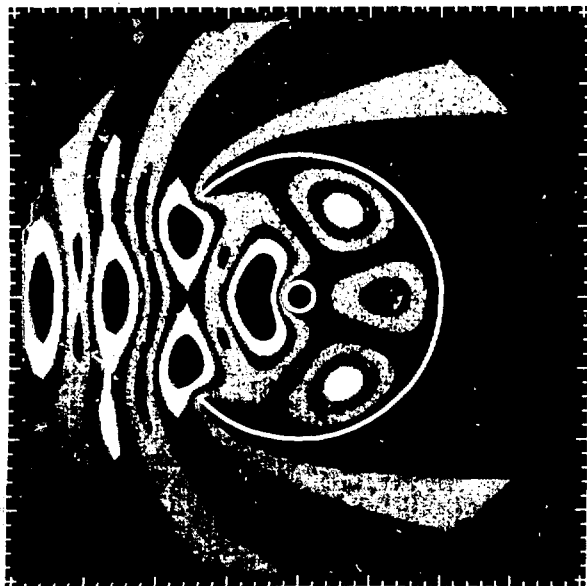
of incident EMP). Hence, the maximum length of wire that can be modeled is limited by the available computer storage. We have solved models with as many as 1200 segments.

Finite-Difference and Finite-Element Methods

Finite-difference and finite-element methods are approximation techniques for studying continuous physical systems or structures. The continuous surface of a structure is broken into discrete elements, interconnected at discrete node points, that can be modeled with numerical techniques. In the finite-difference method, the surface is cut into rectangles, squares, or cubes. In the finite-element method, in contrast, the surface can be divided into irregular shapes, enabling structures or objects to be defined much more accurately.

Finite-difference and finite-element, time-domain, computer programs are the most promising numerical tools, particularly for modeling interior coupling. At present, it is possible to model cubic objects 20 wavelengths on a side with 10 samples per wavelength. Such programs can thus be applied to objects as complex as cavities having multiple apertures and interior cables. Lossy dielectric materials can also be modeled. Currently, such tools can predict generic system responses for modestly complex test objects—those with a noncanonical exterior and interior geometries connected via apertures and seams with simply routed interior bulk cables. These tools can represent objects with a far higher degree of complexity than those addressable by formal analysis. They can be extended to treat more complex and more realistic interior geometries, for example the routing and branching of interior cables. Recent work at LLNL and elsewhere on finite-element and finite-difference codes has yielded results that confirm their power in handling complex geometries.

Finite-difference methods. These techniques directly solve Maxwell's curl equations in the time domain. They have been successfully used in solving one-, two-, and three-dimensional problems. Through this approach, one can address

problems involving conducting, dielectric permeable, anisotropic, and nonlinear media. Irregular scattering surfaces and objects with edges, shadow regions, cavities, and apertures have been modeled with various degrees of success.

In particular, we used a time-domain, finite-difference code[5] to predict the interior coupling response of a wire inside a sheet-aluminum cylinder 1 m tall that was divided internally into one or two cavities with an aperture connecting the interior to the exterior. The code agreed well with experimental measurements to about their 3-GHz limit. Currents measured at the base of the wire were highly resonant, and the code predictions matched these resonances in amplitude (typically to within ±3 dB) and frequency (typically to within ±3% and occasionally to within ±6%).

The specific geometries we considered included an aperture 7.5 by 3.75 cm located at the base of the cylinder, oriented for direct illumination by a transient pulse of the type used experimentally (small corrections were made for the differences between the experimental pulse and the smoother, analytically described pulse used for the

Fig. 5

In this two-dimensional space, the horizontal axis represents object complexity and the vertical axis computational complexity. The applicability of finite-difference and finite-element computer codes extends down to bulk cables, and hybrid techniques must be implemented with transmission-line models down to the individual cable currents.

17
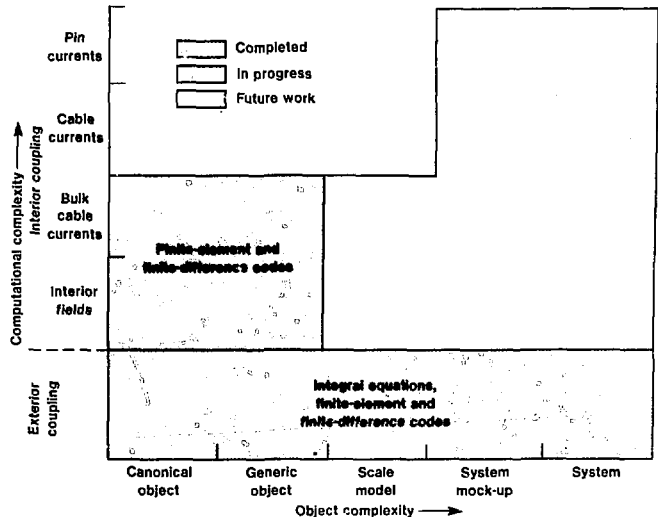
code). Geometric variations in both the test object and the model included:

● Five wire locations within the cylinder.

● Wire terminations (short and open at the top, always shorted at the bottom).

● Cavity height (22.5 and 30 cm).

● One or two cavities (22.5- and 30-cm cavities connected by a 2.5-cm² hole).

This work validated the three-dimensional, time-domain, finite-difference code for predicting interior-coupling responses, as shown in Fig. 6, where the predicted and laboratory-measured power density of the current at the base of a wire at the center of the cavity is plotted as a function of frequency.

However, the conventional finite-difference approach does have limitations. First, objects whose shapes and surfaces are not natural to the coordinate frame of reference are typically modeled with stair-step approximations. Second, the typical use of explicit finite-difference methods imposes potentially severe restrictions on modeling small spatial details. This is because the time steps are proportional to the smallest zone dimensions used to approximate the object or structure of

interest. Finally, large, three-dimensional simulations can tax the largest, fast computers currently available, such as the Cray-1 or the Cyber 205.

Finite-element methods. Recent work at LLNL has applied newer finite-element techniques to solve coupling problems.[6] This approach seeks to weaken the first and second limitations mentioned above. Figure 7 indicates how curved objects such as cylinders can be much more accurately approximated by using irregularly shaped, finite elements. We have also also introduced the use of implicit numerical methods that do not have the time-step constraints of typical explicit finite-difference methods. These methods permit the use of the very small zones, which are needed to model small objects and details accurately.

Figure 8 shows the result of applying our finite-element techniques to study the coupling, scattering, and interaction of an electromagnetic plane-wave pulse with a cylinder having a slot aperture. As expected, the points of maximum field intensity lie near the edge of the aperture. These new applications show promise for achieving greater resolution and accuracy in electromagnetic coupling, scattering, and interaction problems.
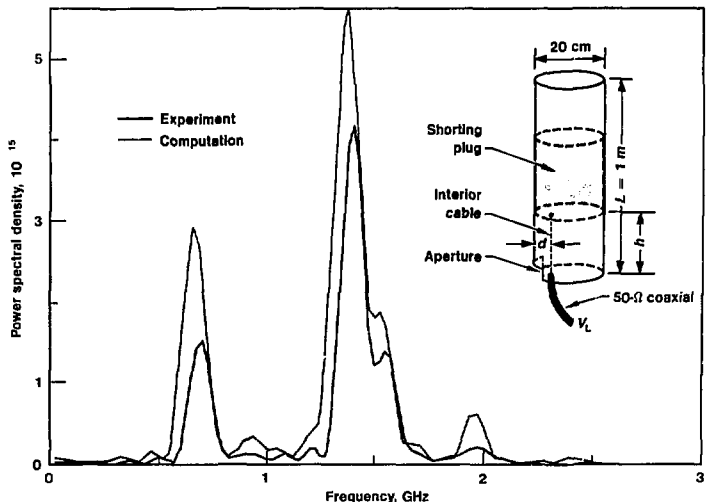

Fig. 6

Power spectral density of the current at the base of the wire for the computation (color) and the experimental (black) response. The inset shows the generic test object. For this case, the wire is along the axis of the cylinder ($d = 10$ cm and $h = 22.5$ cm).

Laboratory Testing

Several time-domain studies using scale models to predict HEMP coupling to systems have yielded very promising results at LLNL and elsewhere.[7] The limits of validity of this technology have yet to be established. Such tools make it possible to deal with levels of complexity far beyond those treatable with numerical analyses. Laboratory model tests can also be used to validate analytical and computational tools.

In principle, many of the EMP laboratory facilities in the U.S. can be used to make interior-coupling measurements. However, only the one at LLNL has been used extensively to make such measurements. Test objects usually include generic and scale models of actual systems. Measurement of generic objects can provide a wealth of information to enhance our understanding of the phenomenology of interior coupling, at least at the generic level. We have performed some scale-model interior measurements and compared the data with full-scale data.

Much more remains to be done before the potential of such laboratory tests can be evaluated.

Transient Testing of Generic Objects

We have been modeling transient electromagnetic pulses for several years at our ElectroMagnetic Transient Range Facility (EMTRF). This approach is fast and cost effective. The scaling law for conducting objects is straightforward: scaling the size downward by a factor F scales up by the same factor the corresponding frequency spectrum of interest. For example, if we seek HEMP coupling information up to 250 MHz on a tactical aircraft 15 m long, the use of a scale model 1.5 m long would require us to obtain laboratory data up to 2.5 GHz.

When studying coupling into systems, we record the time-response using a high-frequency sampling oscilloscope, which permits immediate assessment of maximum impulse voltages and their potential threat to electronic systems. On-line signal-processing facilities provide the Fourier spectrum of the
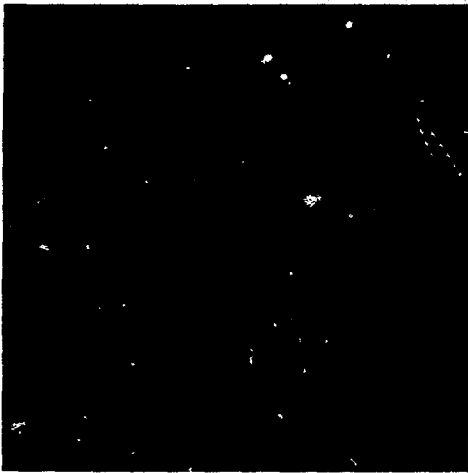

Fig. 7

Finite-element zoning of a cylinder, using irregularly shaped elements. Curved objects such as cylinders can be much more accurately approximated by this technique than by finite-difference methods.
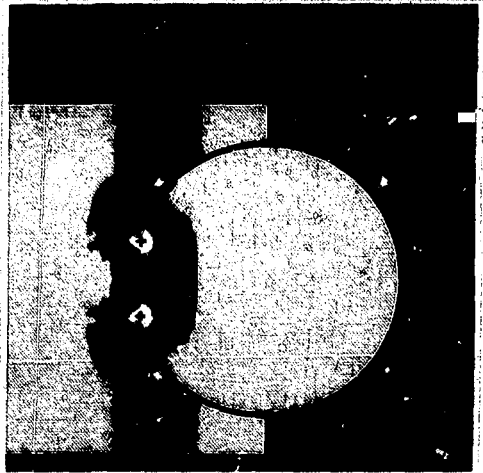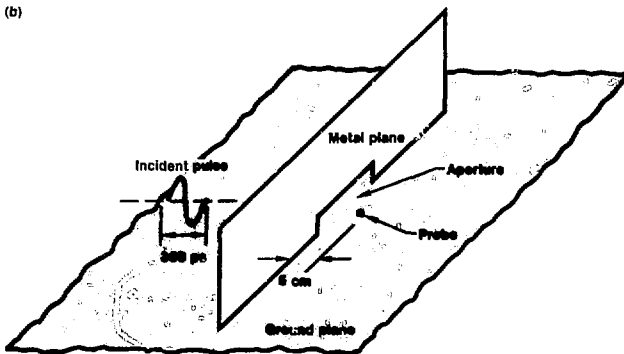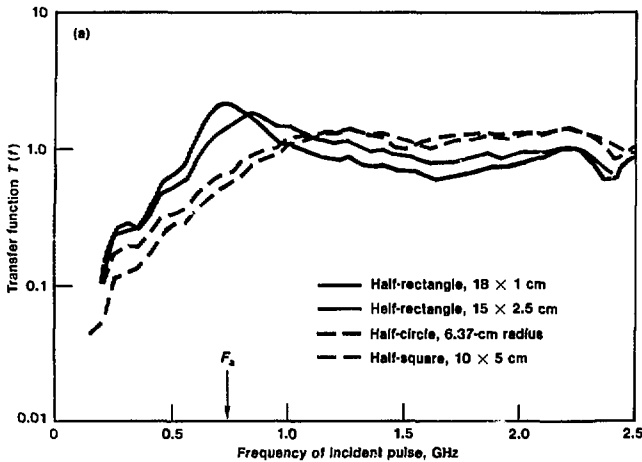

Fig. 8

Finite-element techniques produced this vector plot of the electric field at one instant of time resulting from the interaction of an electromagnetic plane-wave pulse with a cylinder having an aperture slot. The crosses indicate points of maximum field intensity.

response. Since most systems exhibit a variety of resonances to a broad-spectrum impulse, it has become most meaningful to compute the power spectral density (PSD) response, which tends to smooth the data observed in the Fourier response while preserving the total energy in the measured spectrum. This smoothing process accounts for the statistical properties of the otherwise jagged Fourier response. With this technique, it is most meaningful to deconvolve the incident pulse and the actual response to yield the response to an impulse having a flat frequency spectrum. This then provides a means of computing the spectrum of the transfer function or the receiving cross section. The latter is defined as the ratio of power received by the sensor to the incident power density. Although we can define other parameters, such as the open-circuit voltage, the short-circuit current, and the gain, the transfer function and the receiving cross section seem to be the most meaningful modes for presenting the data in most applications.

For example, Fig. 9 shows the transfer function $T(f)$ measured by a sensor that detects the time rate of change of the electric-field displacement for apertures of several different shapes in a metal plane.[7] (Including their mirror images, the apertures were rectangular, circular, and square.) All the apertures were chosen to have the same perimeter value (20 cm) when the total image is included. The onset of the most significant coupling occurs when the perimeter of an aperture, including its mirror image, equals one wavelength. In this case, the corresponding frequency is $F_a = 0.75$ GHz. For long, narrow slots, the response peaks at F_a; for circular or square apertures, the response approximates that of a simple, high-pass filter having a transfer function near unity. Somewhat above F_a, the radiation simply "shines" through the apertures.

Scale-Model Tests

Exterior and interior coupling phenomena have been measured on scale models of ships and aircraft. Exterior-coupling data have been extensively validated over the past few years, both at LLNL and elsewhere, thus establishing the utility of this technology. In a few instances, the LLNL data on interior coupling have been compared with full-scale measurements, and early assessment of the predictive capability of the model data is encouraging. The main difficulty at present is the poor state of our understanding of interior coupling phenomenology, which makes the fidelity of the scale model's interior structure and cabling layout quite problematic. To investigate this problem, we have compared simulated HEMP data obtained from scale models with the

Fig. 9

(a) Transfer functions for various horizontal apertures in a metal plane, measured by a probe that detects the time rate of change of the electric field displacement. (b) Arrangement of the experiment. The onset of significant coupling through the apertures occurs when the distance around the aperture's perimeter, including its mirror image, is one wavelength.

results of experiment on the actual systems.

H.M.C.S Huron. At our EMTRF, we have measured simulated HEMP responses of a 1/48-scale model of H.M.C.S. *Huron,* a Canadian destroyer that was being tested at the U.S. Navy's EMPRESS facility at the time, so that comparative data were available. The model was constructed on the basis of photographic information and engineering data. The main mast and the cable routings down the mast were modeled fairly accurately. The internal routing of the mast cables into the various equipment compartments was also modeled.

The transient data obtained at our facility were extrapolated to the full-scale simulator environment at the EMPRESS facility. Table 1 summarizes the interior-coupling measurements. We have included only those where a one-to-one comparison can be made. We found that:

• Time-domain peaks agree within ±6 dB and only occasionally exceed ±10 dB. The *Huron* scale-model data are overdamped compared to the actual ship measurements.

• A 2-MHz response peak that can be associated with the length of the mast is typically reproduced.

A-7 Aircraft. We constructed and tested in the EMTRF a 1/10-scale model of the U.S. A-7 attack aircraft for both exterior and interior coupling (Fig. 10). The major structural details of the plane's interior were modeled, as were 14 wires simulating the main cable bundles. We compared the EMTRF results with exterior coupling data obtained at various test points on an actual aircraft at the Air Force's Horizontally Polarized Dipole (HPD) EMP simulator at Kirtland Air Force

Table 1 Measurements of EMP-induced currents in internal cables on H.M.C.S. *Huron* at the U.S. Navy's EMPRESS simulation facility and on a scale model at LLNL's EMTRF.

	Ship		Model	
Location	Frequency component, MHz	Peak amplitude, A	Frequency component, MHz	Peak amplitude, A
Communication room 1	2, 6	15	2, 8	17
Communication room 2	2, 4	1.5×7^a	2, 4	24

[a]Seven cables were installed on the ship, but only one was modeled. Had the other six cables carried currents of the same order, the total measured current would have been comparable to the predicted current.

Fig. 10

View of an A-7 scale model in LLNL's Electromagnetic Transient Range Facility (EMTRF). The fusilage is 1.4 m long.

Base, Albuquerque. Agreement was very good. One such comparison for test point 2 is shown in Fig. 11.

Although we recorded the data on all 14 cables in the aircraft, we could make a one-to-one comparison at only four internal locations (Table 2).

Figure 12 shows the frequency-domain comparisons for interior cable No. C1. The histogram distribution of cable-bundle currents at the HPD simulator are shown in Fig. 13, together with the span in current amplitudes measured on all 14 cables in the scale model. We conclude from these results that:

- Exterior measurements are quite reliable for both time history and peak quantities.

- Interior peak currents from the scale model are on the whole larger, probably because most cable runs modeled were long, and there was no deliberate impedance loading from cable to ground.

- The frequency behavior of interior current responses seems to be reproduced.

Conclusions

The phenomenological approach to HEMP coupling complements system testing. Because current test facilities are limited with regard to frequency content, wave polarization, and angle of incidence, it will not be possible in the foreseeable future to conduct full-scale system tests of all values of environmental threat parameters. Consequently, we can at present simulate only a very small subset. The most critical threat parameters can be identified by phenomenological investigations. Should it prove infeasible to test for these, analytical tools can provide a measure of how much the system is understressed (that is, how far the actual stress parameters are from the desired ones) and how to extrapolate systematically from one set of environmental parameters to another. Furthermore, HEMP phenomenology can identify the set of system parameters that most critically affects the system response.

The limitations of full-scale system testing (that is, the constraints on sensitivity tests) obstruct a cost-effective approach to hardening systems against HEMP. The resulting lack of knowledge has led some in the HEMP hardening community to propose expensive hardening of exterior envelopes. However, given sufficient understanding of coupling phenomenology, a far less expensive approach that relies on distributed hardening may prove appropriate and adequate.

Phenomenological studies should focus on stress parameters (especially those that directly cause failure) and on their relationship to the environmental parameters. The evaluation of the
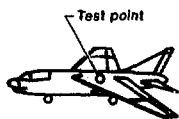

Fig. 11

Time histories of the exterior current measured at test point 2 on (a) an actual A-7 aircraft at the Air Force's HPD EMP simulator and on (b) an A-7 scale model at our EMTRF. The peak current for the aircraft is 180 A/m and for the scale model 190 A/m.
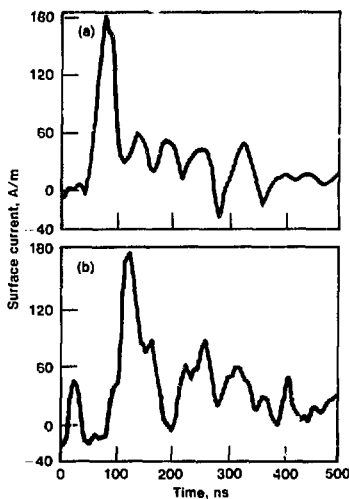
Table 2 Results of internal EMP coupling experiments with an actual A-7 aircraft at the U.S. Air Force's HDP simulation facility and with a scale model at LLNL's EMTRF.

| Cable No. | Pathway | Induced current, A | |
		Aircraft	Model
C1	Left avionics bay to Pylon 1	6.5	8
C2	Nose to tail	4.0	10
C3	Left avionics bay to horizontal tail	6.0	18
C4	Right cockpit to right avionics bay	0.4	15

transfer function, which relates the stress parameters to the environmental parameters for given system parameters, can have an important impact on developing an understanding of the behavior of the stress parameters. In particular, it enables us to systematically investigate other means of inducing the stress parameters (other than a free-field simulator) After all, the fidelity of a simulation-induced stress parameter to a threat-induced stress parameter is of greater importance than the reproduction of the entire threat environment.

Knowledge thus gained can help prepare a credible and cost-effective test protocol for validation testing for system hardness. By identifying the most critical stress parameters ahead of time, the required number of data acquisition points during full-scale system test and associated costs can be reduced.

Our methodological approach combines analytical, computational, and laboratory techniques in a complementary way to take advantage of their separate strengths. The laboratory experiments make use of statistical experimental design principles to ensure that the various techniques are used with maximum efficiency.

Predictive tools for exterior coupling are adequate. For interior coupling, however, such tools are in their infancy. Approaches such as formal analysis, computer models, and laboratory experimentation show great promise. Formal analytical techniques can treat simple canonical shapes and can help develop engineering rules of thumb. Computer models are a promising tool, as they can be used to treat complex objects with arbitrary shapes, dielectrics, and cables, and multiple apertures. Laboratory tests can expand the domain of investigation even further. ∎

Notes and References

1. The modeling of EMP damage to semicor ductors is described in the November 1983 Energy and Technology Review (UCRL-52000-83-11), p. 20.

2. R. Ziolkowski, W. A. Johnson, and K. F. Casey, "Applications of Riemann-Hilbert Problem Techniques to Electromagnetic Coupling through Apertures," Radio Science, November/December 1984.

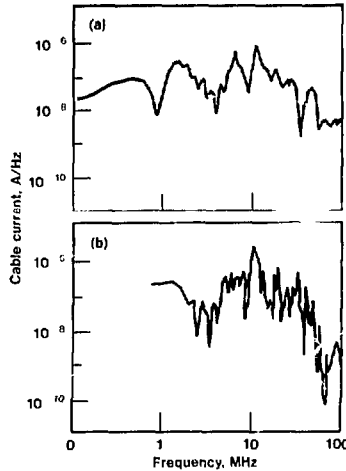3. H. S. Cabayan et al., Phenomenological Investigations in High Altitude EMP (HEMP).

Fig. 12

Frequency domain for interior cable No. C1 in Table 2, measured on (a) an actual aircraft at the HPD simulator and (b) a scale model at our EMTRF. The peak current is 3 A for the aircraft and 6.5 A for the scale model.
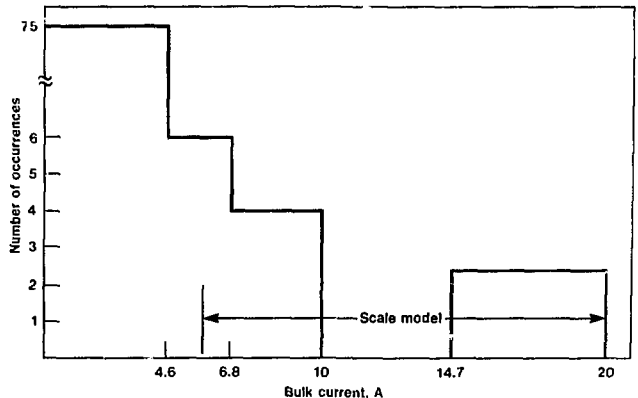

Fig. 13

Histogram of cable-bundle currents measured an an actual A-7 aircraft at the HPD simulator. Also shown is the range of current amplitudes measured on all 14 cables in a scale model in our EMTRF.

Lawrence Livermore National Laboratory, Rept. UCID-20135 (July 1984).

4. G. J. Burke and A. J. Poggio, *Numerical Electromagnetics Code (NEC)—Methods of Moments, Part I: Theory, Part II: Code, Part III: User's Manual*, Naval Ocean Systems Center, San Diego, California, Rept. NOSC TD-116, July 18, 1977 (NEC-1), revised January 2, 1980 (NEC-2).

5. K. Kunz *et al.*, *Experimental Validation of Time Domain, Three-Dimensional, Finite Difference Techniques for Predicting Interior Coupling Responses*, Lawrence Livermore National Laboratory, Rept. UCID-20246.

6. N. Madsen and J. Peterson, "Time Domain Finite Element Methods for EMP Coupling," presented at 1984 NEM Conference, Baltimore, Maryland. See also Lawrence Livermore National Laboratory, Rept. UCRL-90117 (1984).

7. R. King *et al.*, *Phenomenology of Electromagnetic Coupling into Electronic Systems*, Lawrence Livermore National Laboratory, Rept. UCID-20215 (1984).

New Radiation Dosimetry Estimates for Hiroshima and Nagasaki

Our new estimates of the neutron and gamma-ray doses received by atomic-bomb survivors at Hiroshima and Nagasaki may have important implications for current radiation safety standards.

Studies of the atomic-bomb survivors of Hiroshima and Nagasaki have provided us with human, whole-body radiation data that are derived from relatively good records, include a wide range of radiation levels and comprise a relatively large statistical sample that includes both sexes, a spectrum of ages, and other representations of a general population. These data have contributed greatly to our ability to quantify the effects of radiation on human beings. Even though the characteristic features of the radiation from atomic bombs are quite different from those of commonly encountered radiation sources, especially x rays, this quantification of the effects of the radiation received by the atomic-bomb survivors has been fundamental in the setting of radiation safety standards (see the box on p. 30).

The usefulness of the epidemiological data from Hiroshima and Nagasaki depends on the accuracy of our estimates

of both the total radiation doses received by the survivors and the relative importance of the neutron and gamma-ray exposure levels. The estimates currently in use, known as T65D (Ref. 1), were supported by measurements made by Japanese laboratories of building-material activation by neutrons and gamma rays in representative locations at Hiroshima and Nagasaki.[2]

Until 1980, it was thought that dose levels received by individual survivors at Hiroshima and Nagasaki were known to a good accuracy, in most cases with only an estimated 30% uncertainty. Then, in August and September of 1980, we announced[3] that the levels of free-field kerma at locations where there were survivors at Hiroshima and Nagasaki should be revised by factors as large as an order of magnitude, as shown in Fig. 1 (see also the box on p. 32). The most important changes are for Hiroshima, where there is an increase in

the total free-field kerma (hereafter simply called kerma) by a factor of three at 2 km and a drop in the proportion of neutrons in the mixed radiation field by a factor of sixteen at 1.5 km.

Although the consequences are still unfolding, an immediate result of the LLNL dosimetry was that atomic-bomb survivor data no longer support large increases in the neutron quality factor, as considered formally by the National Council on Radiation Protection and Measurements (NCRP) in 1980. (The neutron quality factor is used in radiation protection to express the biological hazard of neutron dose relative to that of gamma-ray dose.) An impetus for that proposed change had come from a study published by Rossi and Mays in 1978 that related leukemia mortality at Hiroshima and Nagasaki to T65D estimates of radiation dose to bone marrow.[4] Their results, summarized in Fig. 2a, show a much higher leukemia risk at Hiroshima than at Nagasaki, corresponding to a high neutron component in the radiation field at Hiroshima, from which these investigators inferred high values of dose-dependent, neutron relative biological effectiveness (RBE) at low doses.

We repeated the procedure used by Rossi and Mays but replaced with our own values (see Fig. 1) the T65D kerma data on which the marrow doses were based. Our results (Fig. 2b) show no difference between the Hiroshima and Nagasaki curves; this is consistent with the low neutron component at Hiroshima as well as Nagasaki, as shown in Fig. 1. Therefore, the leukemia experience at Hiroshima and Nagasaki no longer admits an inference of large neutron RBE. This plot for leukemia, and plots like it for other biological endpoints such as chromosome aberrations, will show changes as the entire dosimetry re-evaluation program continues. However, there is at present no accepted evidence to suggest that the curves for the two cities will again appear to separate by an amount greater than the inherent uncertainties in the data.

Additional Studies

Since 1980, a specially appointed committee of the U.S. National Academy of Sciences, chaired by Professor Frederick Seitz of Rockefeller University, with Professor Robert Christy of the California Institute of Technology as primary consultant, has been studying the radiation fields at Hiroshima and Nagasaki in cooperation with a companion group in Japan chaired by Professor Eizo Tajima of the Japanese National Nuclear Safety Commission. In addition, various symposia and workshops[5-7] suggest the broad basis for investigations of the revised dosimetry initiated by our reports of 1980 and 1981.

The Los Alamos National Laboratory has made an improved estimate of radiation emissions from the Little Boy bomb, dropped on Hiroshima, which results in a downward adjustment at all distances of the LLNL values in Fig. 1a by 33% for neutrons and by 6% for gamma rays.

The Oak Ridge National Laboratory (ORNL) has advanced several alternative dosimetries, the most recent of which[8] confirms these adjusted values to roughly ±30%, neglecting a continuing controversy over the yield at Hiroshima. (This controversy, whether the Little Boy yield was 12.5 kt or 15 kt, is still unresolved, but the present trend is

Fig. 1

LLNL estimates of free-field tissue kerma at (a) Hiroshima and (b) Nagasaki. Earlier estimates, known as T65D, are also shown. Our dose estimates are based on (1) our use of the Los Alamos National Laboratory's estimates of the bomb output, (2) our calculations of neutron and gamma-ray transport through the atmosphere (based on validated air-over-ground calculational tools, validated air cross sections, and estimates of atmospheric conditions), and (3) a comprehensive evaluation of existing test data on delayed gamma rays. The most remarkable change in the dosimetry is that now the neutron kerma at Hiroshima represents a small fraction of the total kerma (neutrons plus gamma rays), as is the case at Nagasaki. (Gamma radiation greatly exceeds neutrons at both cities.)

26
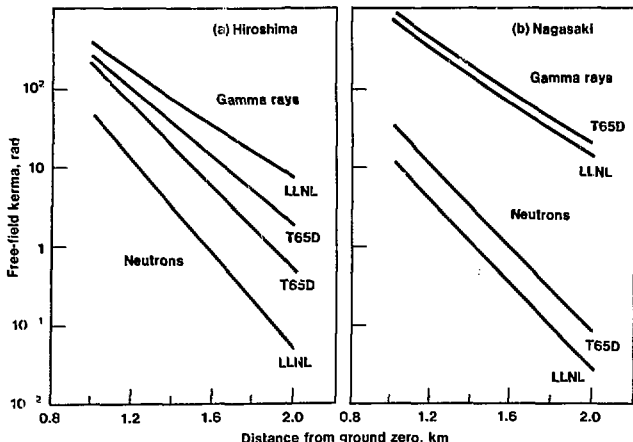
toward agreement at about 15 kt, which we used for obtaining the kerma values in Fig. 1a.)

To date, however, no satisfactory alternative has been offered that would replace our best estimates. Therefore, comparisons here with other relevant data will be made to the Fig. 1 values as reported in 1980 and elaborated in 1981,[9] adjusted for Hiroshima to reflect the improved radiation-emission estimates as just described (that is, reductions of 33% and 6%). We are continuing other calculations that either will confirm the Los Alamos radiation-emission calculations or will establish necessary adjustments to them.

D escription of Bombs

The Little Boy bomb (Fig. 3a), exploded 570 m above Hiroshima at 0815 hours on August 6, 1945, generated about 15 kt of yield from fission of uranium assembled by a very large metal mechanism in a gun arrangement. The Fat Man bomb (Fig. 3b) was exploded 503 m above Nagasaki at 1058 hours on August 9, 1945 and generated 22 kt of yield, mostly from plutonium assembled by a high-explosive implosion. Each of the bombs weighed 4 to 5 tonnes, of which the nonfissioning assembly material constituted a thick blanket surrounding the fissioning core. Neutrons and gamma rays generated in the core had to pass through this thick blanket to reach the atmosphere.

Although there are several reasons for the various errors in the old dosimetry system (T65D), of which two have major significance, the reason for the largest error is the assumption that neutrons that had passed through the two different blanket materials penetrated the atmosphere equally well. (Account had been properly taken of the reduced intensity of emitted high-energy neutrons, using a bare-uranium-metal reactor source for comparison.) However, the number of neutrons actually penetrating to a particular distance depends on source neutrons above a particular energy. The energy required to penetrate increases with the distance, so that the neutron intensity as a function

of distance depends on the details of the source intensity as a function of energy. Now, the high-energy, atmosphere-penetrating part of the emitted Little Boy spectrum falls off rapidly as energy increases as a result of multiple, inelastic neutron collisions with the metals in the thick gun assembly during passage from the fissioning core to the atmosphere.
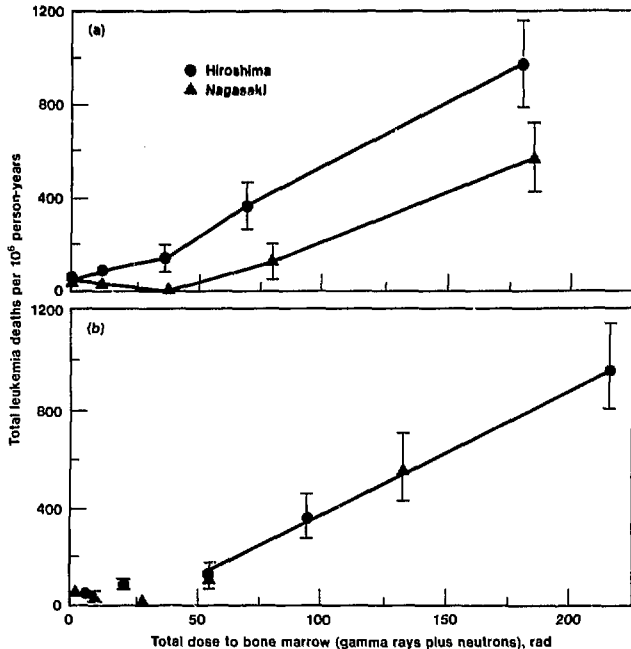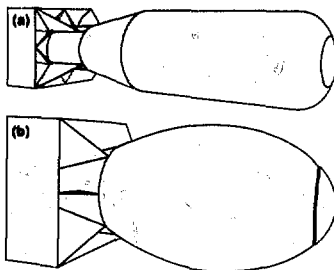

Fig. 2

(a) Results of a 1978 study by Rossi and Mays on leukemia deaths at Hiroshima and Nagasaki.[4] These investigators used available data that relate leukemia mortality among bomb survivors to the T65D free-field kerma adjusted for attenuation by structural shielding and by the body's self-shielding. These results indicate that leukemia mortality as a function of total (gamma-ray plus neutron) dose to the bone marrow varies significantly between the two cities. They postulated that this difference must have been caused by the much higher neutron component in the T65D Hiroshima dose (compared to that for Nagasaki). Accordingly, to reconcile the difference, they deduced very high values of dose-dependent relative biological effectiveness (RBE) for neutrons. (b) We have repeated the procedure used by Rossi and Mays but have replaced the T65D-based kerma data with our own values (from Fig. 1), adjusted (as a first approximation) in accordance with the same structural and body-shielding factors used by Rossi and Mays. The effect of substituting our doses is to eliminate the differences between the Hiroshima and Nagasaki curves and thereby to eliminate the rationale for inferring from these data a neutron RBE much larger than one. (The error bars on leukemia mortality represent one standard deviation based on the sample size. The uncertainties for dose values are not shown on this figure.) Other subsequent renditions of these data, including some at LLNL, permit the same conclusion to be drawn.

The high-energy, penetrating part of the emitted Fat Man spectrum actually falls off less rapidly as energy increases than does the spectrum leaving the fissioning plutonium core. (This phenomenon, caused by the hydrogen in the thick layer of high explosive, is common in light-water reactors, where it is called "spectral hardening.")

Figure 4 shows the energy distribution of the neutrons exiting Little Boy with kinetic energies large enough to determine the neutron kerma beyond 1 km from ground zero, where most survivors were located. In this figure,

various estimates of the Little Boy energy spectrum are compared with the spectrum from a bare-uranium-metal reactor. Although not shown here, the calculated emission spectrum from the Fat Man bomb has a still larger proportion of higher-energy neutrons (relative to those at the largest energies in Fig. 4) than even a bare reactor as a result of the spectral hardening phenomenon. Therefore, atmospheric penetration by neutrons must be very different for the two bombs. In fact, the resulting 30% difference in dose e-folding length (a measure of atmospheric attenuation) for the two bombs generates the differences between T65D and LLNL shown in the neutron curves for Hiroshima in Fig. 1.

As the design laboratory for Little Boy and Fat Man, Los Alamos has provided detailed, state-of-the-art computer calculations of the emission spectra and intensities from both bombs. In addition, they have recently reassembled an exact replica of Little Boy, largely from spare parts produced for the original bomb, on which several experimental teams have made exhaustive emission measurements.[10,11]

Figure 4 also shows the one-dimensional Los Alamos calculations that we used to generate Fig. 1, the more recent two-dimensional Los Alamos calculations discussed previously, and early measurements made on the three-dimensional Little Boy replica by Robitaille and Hoffarth[12] of the Defence Research Establishment, Ottawa (DREO), Canada. Several other groups have confirmed the DREO data shown in Fig. 4, including measurement teams led by Hoots and by Griffith at LLNL. These teams generated an improved description of the angular dependence of the spectra (resulting from the cylindrical symmetry of the gun assembly) and also measured neutron kerma as a function of distance up to 0.5 km[13–15]. The two e-folding lengths derived from these two independent sets of LLNL distance data agree to 6% with our calculated value, which is based on a recent adaptation of the calculation that generated the values in Fig. 1.[16] Static calculations made by Los Alamos in 1984, using the same

Fig. 3

The atomic bombs dropped on Japan in August 1945. (a) Little Boy, detonated at Hiroshima, was 304 cm long and 71 cm in diameter. (b) Fat Man, detonated at Nagasaki, was 325 cm long and 154 cm in diameter. The bombs weighed 4 to 5 tonnes, were detonated roughly 0.5 km above the ground, and generated about 15 to 20 kt of high-explosive equivalent energy.
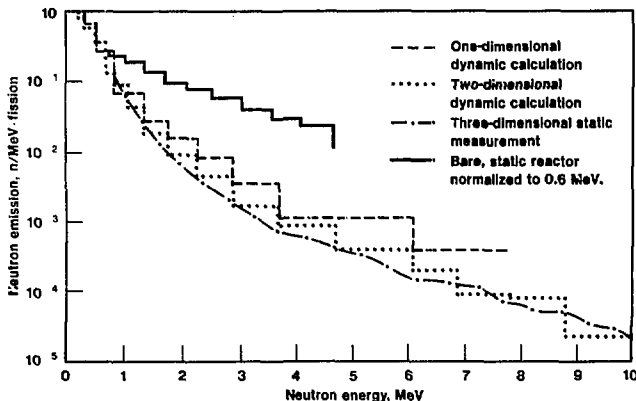

Fig. 4

One- and two-dimensional calculations of the neutron energy spectrum from the exploding Little Boy (Hiroshima) bomb, compared with measured emissions from (the static, three-dimensional) Little Boy replica operated as a reactor. Also shown for contrast is the spectrum from a bare reactor. The intensities shown are for neutrons that have kinetic energies sufficient to penetrate the atmosphere and to determine the neutron kerma beyond the 1 km from ground zero, where most of the survivors were located.

transport representation as in the previous dynamic calculations, lie somewhat lower than the dynamic results shown in Fig. 5 and agree quite well at all energies with the measured (static) data from DREO and LLNL. Except for this modest dynamic effect resulting from geometry changes during the time that neutrons are passing from the core to the exterior, the Little Boy radiation emission is very well known.

Transport Calculations

We have estimated the accuracy of deep-penetration, air-over-ground radiation transport calculations used to generate the kerma values in Fig. 1 to be better than 25 to 30% by comparison with all known pertinent measurements.[17] However, the most modern and carefully done measurements, carried out at the Aberdeen Proving Grounds by international teams of experimenters, have recently benefited from updated measurements by DREO. Table 1 shows a composite of the most up-to-date results for a bare-uranium-metal reactor, with spectral indications that this kind of agreement could be expected for Little Boy and Fat Man sources as well as for these bare reactor sources. At least half of the somewhat larger disagreements of the neutron kerma values at 0.3 and 0.4 km are attributable to the effects of nearby trees at Aberdeen Proving Grounds that were not modeled in the calculations. In general, agreement to about 15% or better seems to be a reasonable expectation for both neutrons and gamma rays to distances of at least 1.6 km. (The absolute accuracies of the data shown in Fig. 1 are not as good, owing to uncertainties in the intensity and spectral composition of the source radiation, in meteorological conditions, and in terrain configuration and composition.)

Contributions from Delayed Sources

One important difference in radiation intensities between a nuclear reactor, as shown in Table 1, and the explosions over Hiroshima and Nagasaki is due to atmospheric rearrangement by

the blast wave (see box on p. 32), which permits delayed gamma rays emitted by fission fragments to contribute roughly half of the total dose even though their contribution would otherwise be small. The gamma-ray data in Fig. 1 include delayed contributions obtained
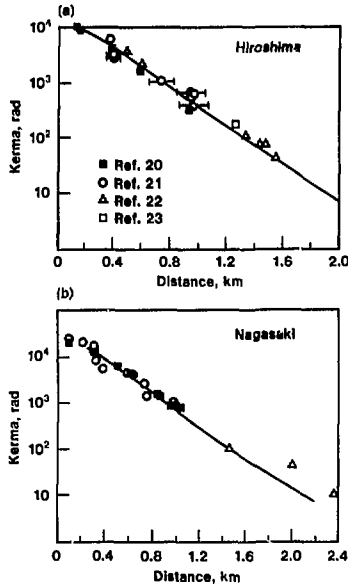
Fig. 5

Comparisons of our gamma-ray kerma estimates in Fig. 1 (curve) with those taken from thermoluminscence dosimetry of roof tiles and face bricks (data points) at (a) Hiroshima and (b) Nagasaki. Our predicted values correspond closely out to 1.5 km. The abrupt discrepancies at 2.0 and 2.3 km at Nagasaki are thought to result from background contributions to the measurements at these great distances.

Table 1 Ratio of LLNL-calculated[a] neutron and gamma-ray kerma to a measurement of radiation from a bare-uranium-metal reactor.[b] (The same calculational methodology was used to generate the curves in Fig. 1.)

Distance from source, km	Calculated kerma/measured kerma	
	Neutron	Gamma-ray
0.100	1.08	1.06
0.170	1.06	0.91
0.300	1.30	0.94
0.400	1.28	0.90
1.080	0.92	0.80
1.618	0.90	0.91

[a]See Ref. 17.
[b]See Ref. 18. The neutron kerma are updated DREO results to 1.08 km and APRD results at 1.618 km. The gamma-ray kerma are averages of several teams' results to 1.080 km and APRD results at 1.618 km.

Radiation Dose to Internal Organs of Atomic-Bomb Survivors at Hiroshima and Nagasaki

When a human body is exposed to neutrons, gamma rays, or x rays, the body tissues absorb energy from the radiation. By studying the harmful effects of this radiation on living tissues and relating the kind and extent of damage to the amount and types of particles present in the radiation, we can determine the safe levels of exposure for humans.

Radiation protection standards are set by boards of experts, such as the International Commission on Radiological Protection (ICRP) and the National Council on Radiation Protection and Measurements (NCRP) in the United States, that use risk estimates based on epidemiological data. These data are analyzed and interpreted by scientific groups such as the United Nations Scientific Committee on the Effects of Atomic Radiation (UNSCEAR) and the successive Committees on the Biological Effects of Ionizing Radiations (BEIR) in the United States. Although standards are based on a variety of epidemiological data, the atomic-bomb survivor experience is paramount because it represents a statistically large sample of whole-body radiation levels. Significant uncertainties remain in the interpretation of these data, including age dependence, variations in latency periods, and whether to rely on incidence or mortality records.

In discussing radiation "dose," a particularly useful construct is known as the kerma. The kerma (kinetic energy released in material) is the kinetic energy imparted to charged particles in a unit mass of material (tissue, in this case) by the radiation particles, including uncharged ones such as neutrons, expressed in rads (one rad is 100 ergs per gram). Thus, the kerma, sometimes called tissue kerma, is the charged-particle energy available for absorption, in contrast to the absorbed dose (also expressed in rads), which is the energy actually absorbed in the tissue per unit mass of material. Typically, the dose in an internal organ or bone marrow is less than the tissue kerma because the body itself shields the organ or marrow.

Estimating the dose to an organ or bone marrow has traditionally been a three-step process (see figure):

- A free-field kerma (or outdoor radiation) value is obtained.
- The free-field kerma value is diminished according to the shielding provided by buildings (if any), resulting in indoor radiation surrounding each individual survivor.
- The shielded kerma is further diminished by attenuation in the body itself and then produces an internal absorbed radiation dose.

The final result is dose, or the energy actually absorbed by an internal organ or bone marrow.

In modern estimates, every detail of the specific nuclear radiation is carried through the two shielding processes before conversion to energy deposited is estimated. Because the details are available at every step, the results are more accurate. Even though our estimates intrinsically permit this detailed development, we stopped with free-field kerma as the point at which the major uncertainties had already been accounted for. (With one exception, noted in the text, shielding attenuations have relatively modest uncertainties.)

The relative biological effectiveness (RBE) of the neutron radiation is the photon dose (gamma ray or x ray) divided by the neutron dose for the same biological damage. In applications, RBE is used as a multiplicative factor on

biological damage due to gamma rays. The higher the RBE, the greater is the biological damage caused by a given dose of neutrons.

The free-field kerma estimates, compiled in 1965 by J. Auxier of the Oak Ridge National Laboratory and called T65D (tentative 1965 dose), were the basis for epidemiological studies against which the radiation safety standards that have been in effect for nearly two decades have been tested.

We have revised the free-field kerma, in some cases by an order of magnitude. J. Marcum, of Research and Development Associates, used our results as additional support for his inferences that building-shielding factors require revision, generally by a factor of 1.6 for attenuation of gamma rays by typical Japanese houses. Still others are revising body-shielding factors (by smaller amounts) because of new details of the radiation field inherent in the revision process.

Outside kerma
(20 krad)

Outside kerma
(100 rad)

Inside kerma
(40 rad)

Internal
dose
(30 rad)
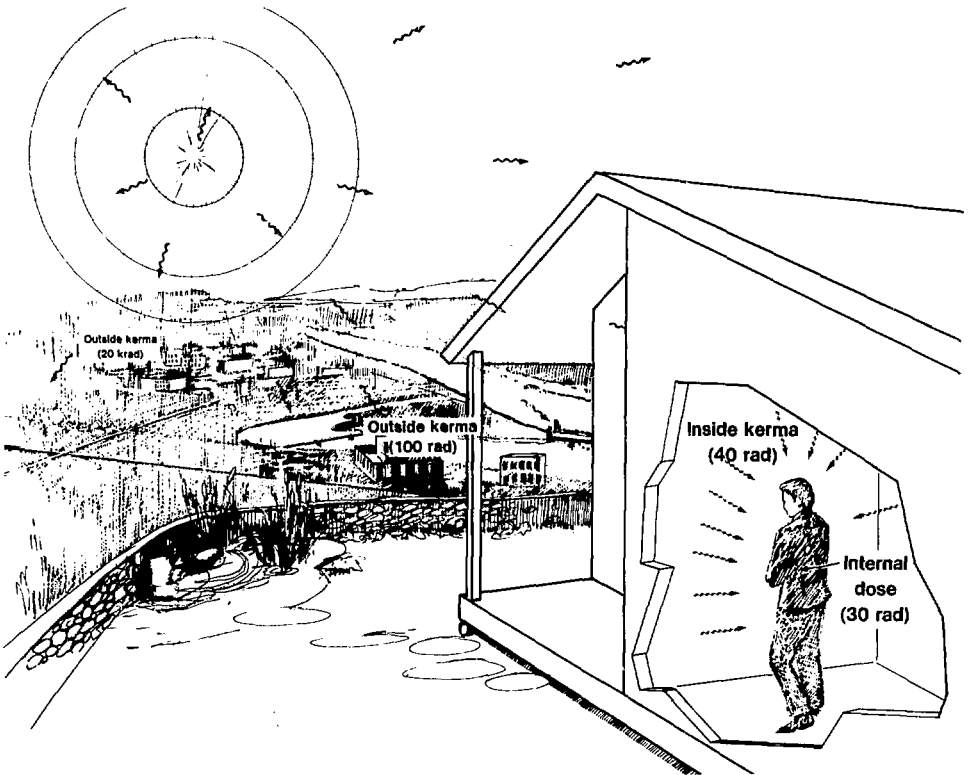
from a model of this dynamic phenomenology based on weapon field tests. We tested the entire calculational chain used for the data in Fig. 1, including this delayed gamma-ray model, by comparing its estimates with measured values from the Fox Event weapon field test (February 1951) in the Ranger series at the Nevada Test Site, which was similar to the Nagasaki explosion. Agreement was within 4% at 1.0 and 1.8 km from ground zero, even though neither the measured nor the calculated estimates can claim such accuracy. A similar dynamic enhancement of delayed fission neutrons also occurs, but by using the same model of the dynamic atmosphere, we have shown this delayed neutron contribution to be negligible.[19]

Thermoluminescence Dosimetry

Thermoluminescence dosimetry of roof tiles and face bricks from buildings irradiated by the bombs in Hiroshima and Nagasaki recently has been extended to distances where most survivors were located, permitting comparisons with the gamma-ray kerma data in Fig. 1. The comparisons shown in Fig. 5, which includes earlier data at shorter distances,[20-23] show a striking confirmation of the essential correctness of our predicted values out to 1.5 km. The abrupt discrepancies at 2.0 and 2.3 km at Nagasaki are thought to result from background contributions to the measurements at these great distances.

Neutron Activation

Measurements of neutron activation of cobalt recently have been reported by Hashizume[24] on samples exposed to the atmosphere on rooftops in Hiroshima, as an extension of earlier measurements made interior to concrete pillars.[20] If a small adjustment, within the limits of uncertainty, is made in the assumed boron content of concrete (not measured at the time cobalt activation was measured inside pillars, but assumed to be similar to that in other contemporary buildings), then the pillar and rooftop data form a consistent set to within 10 to 15%, in the sense

Sources of Radiation at Hiroshima and Nagasaki

In estimating the radiation dose received by any particular survivor of the Hiroshima and Nagasaki atomic-bomb explosions, it is necessary to know where the person was with respect to the detonation. Most of the survivors were about 1 km or more from ground zero. Of all the types of nuclear radiation emanating from a fission explosion, only neutrons and gamma rays can penetrate the atmosphere to such distances, and then only those that are relatively energetic. Thus, it is also necessary to know the detailed characteristics of the radiation source, including energy spectrum.

Neutrons and gamma rays emanated from the fission explosions at Hiroshima and Nagasaki with two distinct time scales, termed prompt and delayed.

Prompt Radiation

Neutrons reaching the vicinity of the ground from the fission explosion may travel directly through the air or may reach the ground after scattering off atmospheric nuclei, especially those of nitrogen and oxygen atoms (Fig. a). A few may scatter from ground nuclei.

Gamma rays reaching the ground from the fission explosion travel directly through the air or are scattered by atmospheric nuclei (or ground nuclei) (Fig. b). Secondary gamma-ray sources are actually generated by prompt neutrons. These sources are primarily prompt-capture gamma rays produced by capture of thermal neutrons by atmospheric nitrogen. The shadings indicate decreasing density of these capture gamma-ray sources as the thermal neutron fluence diminishes with distance from the source.

Figure (a):
Neutron source
Scattered neutron
Measurement point
0.5 km

Figure (b):
Direct gamma-ray
Secondary gamma-ray sources
Scattered gamma ray
gamma-ray source
2 km

Figure (c):
Shock wave
Near vacuum
Debris cloud

Delayed Radiation

The rising debris cloud emits delayed neutrons and gamma rays on a time scale of tens of seconds after a nuclear explosion (Fig. c). This delayed radiation would generate, in an ambient atmosphere, doses along the ground that are weaker by orders of magnitude than those from prompt radiation. Because the blast wave locally rearranges the atmosphere, however, it attenuates delayed radiation much less than does the static atmosphere seen by the prompt radiation. As a result, the delayed gamma-ray term is nearly equal in magnitude to the prompt term for gamma-ray kerma. (For neutron kerma, the delayed term is much smaller than the prompt term.)
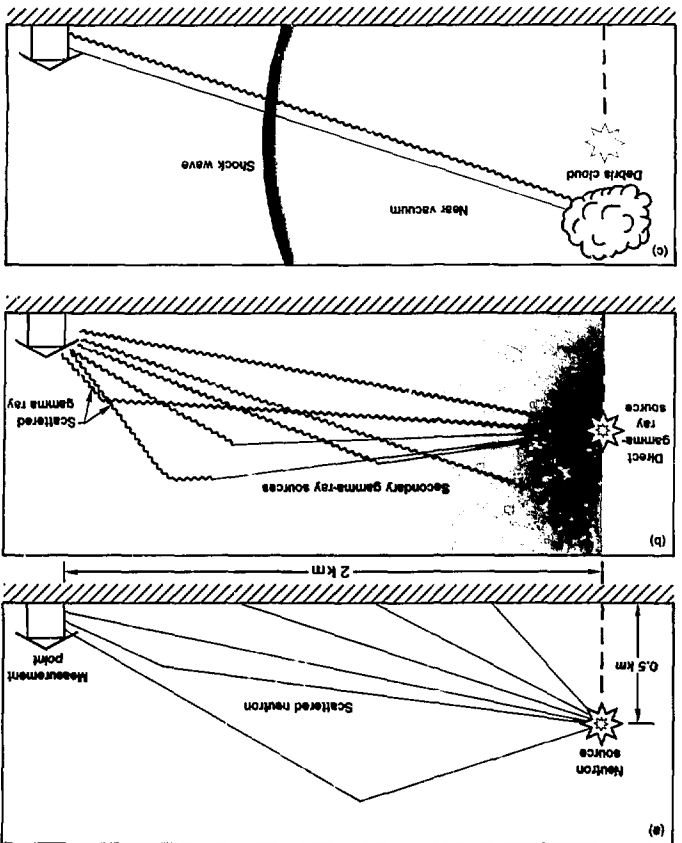
that the two sets relate to each other as predicted by calculations and have a parallel behavior. However, in absolute terms, these data show these iron-ring and boron-adjusted pillar calculations, when compared with experiment, to be high by 15% near ground zero, low by 40% at 0.5 km, and low by a factor of four at 1 km. This striking lack of agreement may be attributable to an unknown deficiency in the description of the source radiation due to dynamic effects during the explosion, an unknown deficiency in the calculated transport of subkilovolt neutrons responsible for cobalt activation, or an unknown experimental problem. However, the same kind of dynamic source deficiency would have to apply to the very different Fat Man as well as to Little Boy, since the Nagasaki pillar comparisons parallel those at Hiroshima. Also, recent work by Woolson and Gritzner at Science Applications, Inc. (SAI) changes the fair agreement of calculated and measured values obtained previously for neutron activation of sulfur[25] at Hiroshima into the excellent detailed agreement shown in Fig. 6.[26] This agreement depends on both the revised sulfur data of Hamada[27] and the angularly dependent energy spectra of neutron emission as calculated by Los Alamos using its two-dimensional model of Little Boy, along with the nonvertical fall of the bomb, and tends to make a dynamic source error unlikely (the replica measurements cited above render a static error highly improbable).
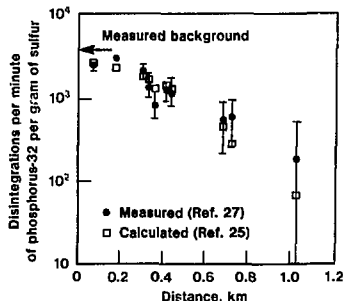

Fig. 6

Measured and calculated neutron activation of sulfur at Hiroshima.

Building Shielding
J. Marcum of Research and Development Associates[28] announced in 1980 improved estimates of the gamma-ray shielding provided by Japanese dwellings. His factor of 1.6, by which previous transmitted gamma-ray estimates are to be reduced, has been recently confirmed by SAI using detailed computer calculations that agree to within 10% with selected values measured at weapons tests inside model buildings.[29] These computer calculations can be used to model in high detail any survivor shielding configuration for which geometry and material records are available.

Conclusions
We have calculated new kerma estimates for survivors of the Hiroshima and Nagasaki bombings that should be considered trustworthy, in part because the greatest departure from previous dose estimates has been explained and in part because of the use of modern validated techniques. Good agreement is obtained with *in situ* measurements of gamma rays. We have applied the Rossi and Mays methodology to these data and find that the results do not support the inference of large neutron RBEs from leukemia incidence.

Large changes from the estimates discussed here are becoming increasingly unlikely as verifying evidence accumulates. However, improvements are expected as a result of the international program currently under way, and the discrepancies noted in cobalt activation must be resolved. It is possible that the absolute accuracy (30%) previously attributed to the T65D dosimetry might eventually be achieved for the new dosimetry.

Quantitative assessment, for each survivor, of radiation sources other than prompt radiation (such as fallout, rainout, induced activation, the food chain, and medical x-rays) may be included as uncertainties or introduced directly as contributions to total dose. (Relatively few survivors are expected to show a significant additional dose from such sources, but the potential importance of

any who do makes these contributions of particular interest.)

As an immediate consequence of the new dosimetry, the utility of atomic-bomb survivor experience in evaluating neutron radiation safety is currently somewhat unsettled. It is expected that its usefulness in evaluating gamma-radiation safety will ultimately be enhanced, but because of the very small proportion of neutrons in the radiation field it probably will not prove suitable as a basis for inferring anything about the human neutron RBE. Profound changes in our understanding of cause-and-effect relationships in radiation exposure may emerge over the next several years as previous discrepancies inhibiting inference are resolved (for example, between human and animal data) and as the quantitative implications of these new causes for the same known effects are traced through step by step. The impact any such changes in understanding might have on radiation safety standards is unpredictable.

The continuing dosimetry studies and subsequent epidemiological revisions present the opportunity to reexamine the records of individual survivors and to correct data explicitly for such matters as body size and orientation, heredity, prior and subsequent major illnesses, and possible selective effects operating at the time of the bombing (for example, the "healthy survivor" effect). At the very least, such revisions will enable the quantification of uncertainties. ⊔

Key Words: atomic bomb—Little Boy, Fat Man; Hiroshima; Nagasaki; relative biological effectiveness (RBE); kerma; radiation standards; radiation—gamma ray, neutron, dose, dosimetry.

Notes and References

1. J. A. Auxier, "Ichiban: Radiation Dosimetry for the Survivors of the Bombings of Hiroshima and Nagasaki," *ERDA Critical Review,* Oak Ridge National Laboratory, Oak Ridge, Tennessee, Rept. TID-27080 (1977).

2. T. Hashizume *et al.,* "Estimation of the Air Dose from the Atomic Bombs in Hiroshima and Nagasaki," *Health Phys.* 13, 149 (1967).

3. W. E. Loewe and E. Mendelsohn, "Revised Dose Estimates at Hiroshima and Nagasaki," *Health Phys.* 41, 663 (1981).

4. H. H. Rossi and C. W. Mays, "Leukemia Risk from Neutrons," *Health Phys.* 34, 353 (1978).

5. V. P. Bond and J. W. Thiessen, Eds., *Reevaluations of Dosimetric Factors, Hiroshima and Nagasaki: Proceedings of a Symposium held at Germantown, Maryland, September 15–16, 1981,* Technical Information Center, U.S. Department of Energy, Rept. CONF-810928 (DE81026279) (1982).

6. *Proc. U.S.-Japan Joint Workshop for Reassessment of Atomic Bomb Radiation Dosimetry in Hiroshima and Nagasaki, Japan, 16–17 February 1983,* (Radiation Effects Research Foundation, Hiroshima, Japan, 1983).

7. *Proc. Second U.S.-Japan Joint Workshop for Reassessment of Atomic Bomb Radiation Dosimetry in Hiroshima and Nagasaki, Japan, 8-9 November 1983* (Radiation Effects Research Foundation, Hiroshima, Japan, 1983).

8. G. D. Kerr, J. D. Pace III, and W. H. Scott, Jr., "Tissue Kerma vs Distance Relationships for Initial Nuclear Radiation from the Atomic Bombs at Hiroshima and Nagasaki," Ref. 6, p. 57.

9. W. E. Loewe and E. Mendelsohn, "Neutron and Gamma-Ray Doses at Hiroshima and Nagasaki," *Nucl. Sci. and Eng.* 81, 325 (1982).

10. *Little Boy Replica Conference at Los Alamos National Laboratory, Los Alamos, New Mexico, September 14, 1983,* Lawrence Livermore National Laboratory, Rept. UCRL-90258 (1983).

11. "Replication of Little Boy I," and "Replication of Little Boy II," special sessions, 29th Annual Meeting of the Health Physics Society, New Orleans, Louisiana, June 3–8, 1984, *Abstracts of Papers Presented at the Meeting* (Pergamon Press, 1984).

12. H. A. Robitaille and B. E. Hoffarth, *Neutron Leakage from "Comet"—A Duplicate Little Boy Device,* Defence Research Establishment, Ottawa, Canada, Rept. 878 (1983).

13. R. V. Griffith, C. J. Huntzinger, and J. H. Thorngate, "Neutron Spectra as a Function of Angle at Two Meters from the Little Boy Assembly," Ref. 11, Paper 142.

14. S. Hoots and D. Wadsworth, "Neutron and Gamma Dose and Spectrum Measurements of the Little Boy Replica," Ref. 11, Paper 143.

15. C. J. Huntziger and D. E. Hankins, "Neutron and Gamma Dose Measurements at Various Distance from the Little Boy Replica," Ref. 11, Paper 144.

16. W. E. Loewe, *Initial Radiation from Tactical Nuclear Weapons,* Lawrence Livermore National Laboratory, Rept. UCRL-90018 (1983). Data given here were adjusted for differences in atmospheric density (adaptation unpublished).

17. W. E. Loewe *et al.,* "Validated Deep-Penetration, Air-Over-Ground, Neutron/Gamma-Ray Transport," *Nucl. Sci. and Eng.* 85, 87 (1983).

18. Measurements by A. H. Kazi *et al.,* U.S. Army Aberdeen Proving Grounds, and by H. A. Robitaille, Defence Research Establishment (DREO), Ottawa, Canada, in A. H. Kazi,

C. R. Heimbach, K. C. Hansen (U.S. Army), and H. A. Robitaille (DREC), "Comparison of Measured and Calculated Radiation Transport in Air-Over-Ground Geometry to 1.6 km from a Fission Source," *Nucl. Sci. and Eng.* **85**, 371 (1983). DRFC data modified in accordance with personal communication from H. A. Robitaille (March 5, 1984).

19. W. E. Loewe, *Hiroshima and Nagasaki Initial Radiations: Delayed Neutron Contributions and Comparisons of Calculated and Measured Cobalt Activation*, Lawrence Livermore National Laboratory, Rept. UCRL-90462 (1984).

20. T. Hashizume e. al., "Estimation of the Air Dose from the Atomic Bombs in Hiroshima and Nagasaki," *Health Phys.* **13**, 149 (1967).

21. Y. Ichikawa *et al.*, "Thermoluminescence Dosimetry of Gamma Rays from Atomic Bombs in Hiroshima and Nagasaki," *Health Phys.* **12**, 395 (1966).

22. T. Maruyama *et al.*, "Reassessment of Gamma Ray Dose Estimates from Thermoluminescent

Yields in Hiroshima and Nagasaki," Ref. 6, p. 122.

23. Y. Ichikawa and T. Nagatomo, "Thermoluminescent Dating and its Application to Gamma Ray Dosimetry," Ref. 6, p. 104.

24. T. Hashizume, "Present Plans for Dose Reassessment Experiments by the Japanese," Ref. 6, p. 7.

25. Personal communication, W. A. Woolson and M. Gritzner, Science Applications Inc., San Diego, California (June 1984).

26. W. E. Loewe, "Calculations and Interpretations of *In Situ* Measurements of Initial Radiations at Hiroshima and Nagasaki," Ref. 6, p. 138.

27. T. Hamada, "Measurement of ^{32}P Activity Induced in Sulfur in Hiroshima," Ref. 6, p. 45.

28. J. Marcum, "Building-Transmission Factors," Ref. 5, p. 179.

29. W. A. Woolson and M. L. Gritzner, *Calculations of the BREN Japanese House Shielding Experiments*, Science Applications, Inc., San Diego, California, Rept. SAI-83-1020 (1983).

MARS: The Mirror Advanced Reactor Study

The Mirror Advanced Reactor Study (MARS) produced a comprehensive conceptual design of a deuterium-tritium-fueled commercial fusion reactor based on the tandem-mirror principle. The configuration described is a 1200-MW_e commercial electricity-generating plant.The MARS machine emphasizes the attractive features of the tandem-mirror concept, including steady-state operation, a small-diameter, high-beta plasma, a linear central cell with simple, low-maintenance blankets, low first-wall heat fluxes (less than 10 W/cm^2), an absence of driven plasma currents or associated disruptions, a natural diversion of plasma impurities, and direct conversion of the energy of end-loss charged particles into electric power. Particular emphasis in this study was placed on the exploitation of the potential of fusion for improved safety, lower activation, and simpler disposal of radioactive wastes compared with fission.

Contact: L. John Perkins (415) 423-6012.

Electromagnetic Coupling of High-Altitude, Nuclear Electromagnetic Pulses

We have used scale models to measure the predicted coupling of electromagnetic fields simulating the effects of high-altitude nuclear electromagnetic pulses (HEMP) on the interior surfaces of electronic components. Predictive tools for exterior coupling are adequate. For interior coupling, however, such tools are in their infancy. Our methodological approach combines analytical, computational, and laboratory techniques in a complementary way to take advantage of their separate strengths. Computer models are a promising tool, as they can be used to treat complex objects with arbitrary shapes, dielectrics, and cables, and multiple apertures. Laboratory tests can expand the domain of investigation even further.

Contact: Hriar Cabayan (415) 422-8871.

New Radiation Dosimetry Estimates for Hiroshima and Nagasaki

Earlier studies of radiation dosimetry for atomic-bomb survivors at Hiroshima and Nagasaki attributed differences in leukemia mortality rates between the two cities to corresponding differences in neutron dosage levels. A high value of estimated neutron relative biological effectiveness (RBE, or level of biological damage caused by neutrons) was accordingly inferred. It now appears that the earlier dosimetry system produced estimates of neutron dose that are high by an order of magnitude. We have applied the new dose estimates to the leukemia data and have found that the results do not support an inference of a large neutron RBE at low doses. Subsequent evidence, discussed here, tends to confirm our analysis within the prevailing uncertainties. As a result, the utility of data on atomic-bomb survivors in evaluating radiation safety standards is problematic.

Contact: William E. Loewe (415) 422-6594.

AAABSTRACTS

Recent Titles

Articles published in recent issues of the *Energy and Technology Review* are grouped below according to their chief sponsors, the Assistant Secretaries of the U.S. Department of Energy. Research funded by other Federal agencies is listed under Work for Others.

ENERGY RESEARCH

MARS: The Mirror Advanced Reactor Study (November 1984)
Uranium Resources and the Development of Fission and Fusion Breeder Reactors (October 1984)
Climatic Warming and Carbon Dioxide (September 1984)
Response of Plants to Increased Carbon Dioxide (September 1984)
Energy-Flow Diagrams: An LLNL Contribution to Energy Analysis (May 1984)
Magma Evolution (May 1984)
Single-Chromosome Gene Libraries of Human DNA (Brief—May 1984)

FOSSIL ENERGY

Computer Simulation of Particulate Flow (May 1984)
Dispersion Tests of Liquefied Gaseous Fuels (Brief—May 1984)

DEFENSE PROGRAMS
Military Application

Electromagnetic Coupling of High-Altitude, Nuclear Electromagnetic Pulses (November 1984)
New Radiation Dosimetry Estimates for Hiroshima and Nagasaki (November 1984)
Supracompression of High-Explosive Detonation Products (October 1984)
Raman Spectroscopy of Shocked Water (Brief—April 1984)
Silicone Cushions for Engineering Applications (April 1984)
Synchrotron-Radiation Research Facility (Brief—April 1984)

LABORATORY REVIEWS

Entering the World of Multiprocessing (October 1984)
Earthquake Safety at LLNL (August 1984)
Geology of the Livermore Valley (August 1984)
Monitoring Groundwater Quality at Site 300 (August 1984)
State of the Laboratory Issue (July 1984)
LLNL in the Developing Livermore Valley (April 1984)

WORK FOR OTHERS
Defense Nuclear Agency

Simulating Nuclear Cratering Events at the Pacific Proving Ground (September 1984)

Nuclear Regulatory Commission

Earthquake-Hazard Analysis for Nuclear Power Plants (June 1984)
Human Factors in Reactor Facility Design (June 1984)
Reactor-Coolant Piping: Realistic Failure Assessment (June 1984)

United States Geological Survey

The Strength of Ice (April 1981)

Disclaimer